Title

A neonatal mouse model characterizes transmissibility of SARS-CoV-2 variants and reveals a role for ORF8

Authors

Bruno A. Rodriguez-Rodriguez[1+], Grace O. Ciabattoni[1+], Ralf Duerr[1], Ana M. Valero-Jimenez[1], Stephen T. Yeung[1,2], Keaton M. Crosse[1], Austin R. Schinlever[1], Lucie Bernard-Raichon[1], Joaquin J. Rodriguez Galvan[1], Marisa E. McGrath[3], Sanjay Vashee[4], Yong Xue[4], Cynthia Loomis[5], Kamal M. Khanna[1,2], Kenneth Cadwell[6,7,8], Ludovic Desvignes[9,10], Matthew F. Frieman[3], Mila B Ortigoza[1,9]*, and Meike Dittmann[1]*

[1] Department of Microbiology, New York University Grossman School of Medicine, New York, New York, NY 10016, USA

[2] Perlmutter Cancer Center, New York University Langone Health, New York, NY 10016, USA

[3] Department of Microbiology and Immunology, Center for Pathogen Research, University of Maryland School of Medicine, Baltimore, MD 21201, USA

[4] Department of Synthetic Biology and Bioenergy, J. Craig Venter Institute, Rockville, MD 20850, USA

[5] Department of Pathology, New York University Grossman School of Medicine, New York, New York, NY 10016, USA

[6] Division of Gastroenterology and Hepatology, Department of Medicine, University of Pennsylvania Perelman School of Medicine, Philadelphia, PA 19104, USA

[7] Department of Systems Pharmacology and Translational Therapeutics, University of Pennsylvania Perelman School of Medicine, Philadelphia, PA 19104, USA

[8] Department of Pathology and Laboratory Medicine, University of Pennsylvania Perelman School of Medicine, Philadelphia, PA 19104, USA

[9] Department of Medicine/Division of Infectious Diseases and Immunology, New York University Grossman School of Medicine, New York, NY 10016, USA

[10] High Containment Laboratories - Office of Science and Research, NYU Langone Health, New York, NY 10016, USA

[+] Co-first authors

*Co-corresponding authors

Abstract

Small animal models have been a challenge for the study of SARS-CoV-2 transmission, with most investigators using golden hamsters or ferrets[1,2]. Mice have the advantages of low cost, wide availability, less regulatory and husbandry challenges, and the existence of a versatile reagent and genetic toolbox. However, adult mice do not robustly transmit SARS-CoV-2[3]. Here we establish a model based on neonatal mice that allows for transmission of clinical SARS-CoV-2 isolates. We characterize tropism, respiratory tract replication and transmission of ancestral WA-1 compared to variants Alpha (B.1.1.7), Beta (B.1.351), Gamma (P.1), Delta (B.1.617.2), Omicron BA.1 and Omicron BQ.1.1. We identify inter-variant differences in timing and magnitude of infectious particle shedding from index mice, both of which shape transmission to contact mice. Furthermore, we characterize two recombinant SARS-CoV-2 lacking either the ORF6 or ORF8 host antagonists. The removal of ORF8 shifts viral replication towards the lower respiratory tract, resulting in significantly delayed and reduced transmission in our model. Our results demonstrate the potential of our neonatal mouse model to characterize viral and host determinants of SARS-CoV-2 transmission, while revealing for the first time a role for an accessory protein in this context.

Introduction

Despite worldwide vaccination efforts and increasing natural immunity, emerging SARS-CoV-2 variants continue to infect and burden the health of millions of people[3]. Past variants of concern include Alpha (B.1.1.7), Beta (B.1.351), Gamma (P.1), Delta (B.1.617.2) and Omicron (B.1.1.529), while Omicron sub-lineage XBB.1.5 currently dominates the first half of 2023[4]. Variants differ in key genes across the viral genome, including Spike (*S*), *ORF1a*, *ORF1b*, Nucleocapsid (*N*), *ORF3a*, *ORF6*, *ORF7a*, *ORF8*, *ORF9b*, Envelope (*E*), and Membrane (*M*). Much attention has been given to changes in Spike, as this envelope glycoprotein is the antigen targeted for most vaccination strategies to date[5] and is key to viral entry into cells[6]. Other key hotspots that accumulate mutations in SARS-CoV-2 variants are accessory proteins, of which SARS-CoV-2 encodes 8, and some serve as antagonists of the antiviral host response, most notably type I interferon production and response[7-9]. Our knowledge of SARS-CoV-2 ORFs stems from inferring functional similarities with SARS-CoV-1 and other Coronaviruses as well as functional studies using ORF cDNA overexpression constructs or full recombinant SARS-CoV-2[10-13]. The high number of SARS-CoV-2 infections coinciding with the appearance of new variants raised concerns about enhanced transmission of these variants, posing considerable ramifications for resolution of the COVID-19 pandemic[14].

Molecular characterization of SARS-CoV-2 variants is essential to our ability to develop appropriate antiviral strategies. Previous studies have characterized SARS-CoV-2 variants by evaluating receptor binding and affinity, antigenic escape and replication dynamics as well as pathogenesis and immune evasion[15,16]. However, comparative

studies on variant transmission and the molecular mechanisms governing variant-specific transmission differences are still scarce. This is partially due to limitations inherent to current animal models, such as ferrets or hamsters. While excellent models for the study of SARS-CoV-2 pathogenesis and transmission[1,2,17], they require special housing, the number of contact animals per index is limiting, they lack species-specific reagents, and have no or limited availability of genetic manipulation to perform mechanistic studies on host factors of transmission. In contrast, mice offer a versatile and readily available genetic toolbox, and reagents are widely available; yet, adult mice do not efficiently transmit respiratory viruses, such as influenza viruses, despite being susceptible to infection[18]. We previously overcame this hurdle for influenza virus by using neonatal mice[18], a model that has been used to study bacterial infection for over 30 years[19,20], and transmission for 7 years[18,20-23]. The model has also successfully been applied by others to study mouse parvovirus transmission[24]. Our previous study revealed influenza virus strain-specific transmission differences, the role of humoral immunity in protection of influenza virus transmission, and the influence of sialidase expression during influenza virus–*Streptococcus pneumonia* co-infection[18]. However, the model is not established for SARS-CoV-2.

Here, we present a neonate K18-hACE2 mouse model that allows for transmission of SARS-CoV-2 between pups of the same litter, and we examine side-by-side the transmission of early and current SARS-CoV-2 variants of concern (VOC). In addition, we characterize the transmission of two recombinant SARS-CoV-2, lacking accessory proteins ORF6 or ORF8. Our study highlights the power of our model to elucidate the dynamics of SARS-CoV-2 variant transmission and provides evidence of an accessory

protein, ORF8, to be critical for SARS-CoV-2 transmission in neonatal mice. Our tractable small animal model will help decipher some of the most critical factors involved in the transmission of SARS-CoV-2.

Results

Neonatal K18-hACE2 mice efficiently support SARS-CoV-2 WA-1 transmission

While influenza viruses readily infect wild-type mice, the ancestral SARS-CoV-2 and the previously clinically important delta variant rely on the human version of the SARS-CoV-2 host cell receptor, ACE2, and cannot engage murine Ace2[25]. In contrast, a number of other SARS-CoV-2 variants acquired specific Spike mutations, most notably N501Y, which allows them to bind murine Ace2[26]. Ultimately, we aimed to compare a panel of variants, from Alpha to Omicron, to the ancestral SARS-CoV-2. With this in mind, we utilized K18-hACE2 mice in our study, which express human ACE2 under the control of the K18 promoter[27].

For SARS-CoV-2, data on transmission in adult mice is scarce, with one study reporting SARS-CoV-2 B.1.351 (Beta) transmission from index mice infected with 5E6 FFU via close contact[3]. Transmission between co-housed mice in the same cage, determined by the presence of viral RNA in or seroconversion of contacts, was 41 and 8%, respectively. Infectious virus was not assessed. Transmission of influenza viruses in adult mice has also been inefficient and inconsistent with transmission events being difficult to reproduce between research groups[18,28,29]. This rendered the adult mouse model an unreliable tool to study transmission of influenza viruses. To determine the

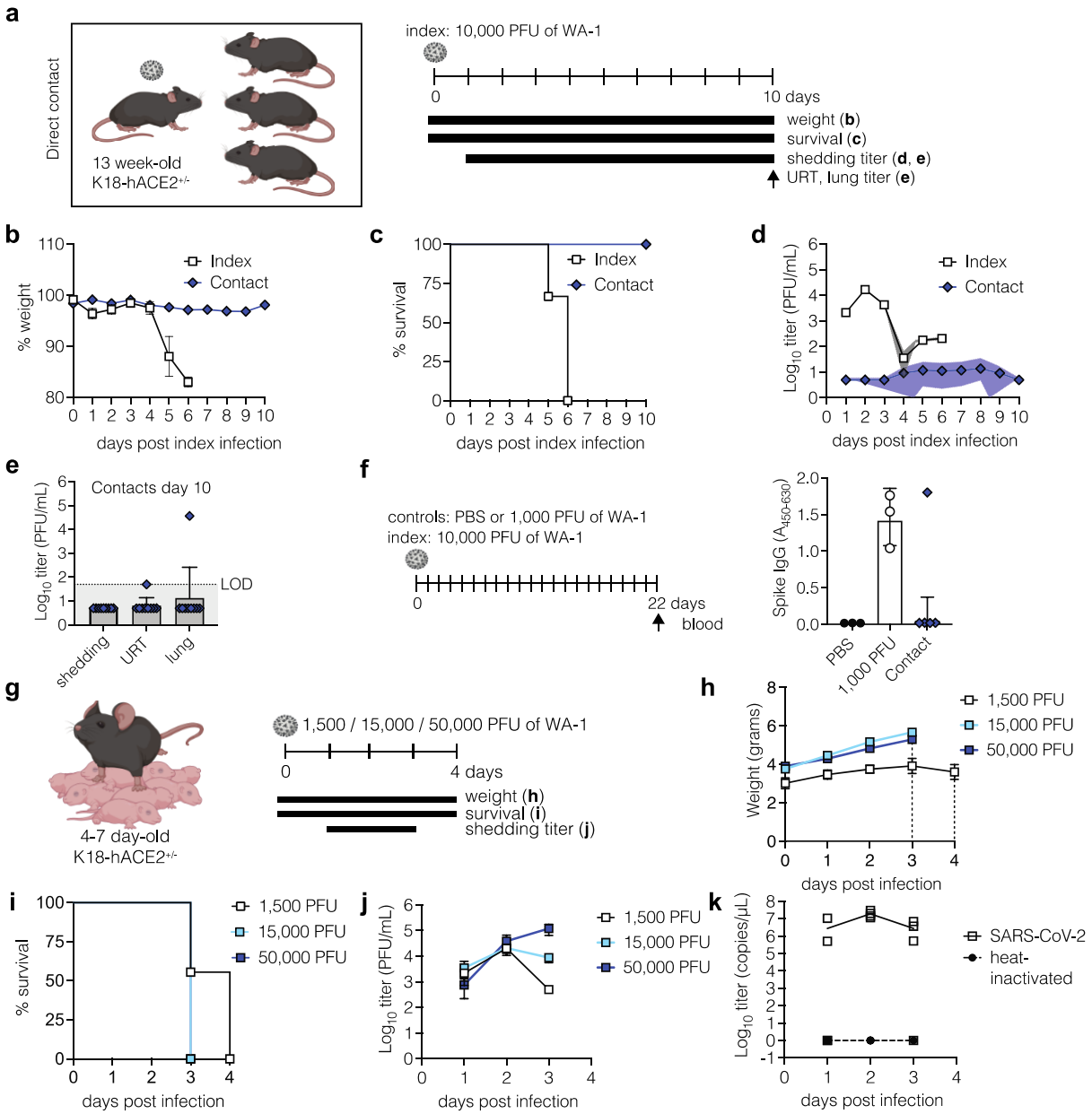

Supplemental Figure 1, related to Figure 1. a, Experimental overview for panels b-e. 13-week-old K18-hACE2$^{+/-}$ mice were infected intranasally with a lethal dose (10,000 PFU) of SARS-CoV-2 WA-1 (index) and cohoused with uninfected littermates (contact) for 10 days at an index:contact ratio of 1:3. Weight and survival were monitored daily. Viral shedding samples were collected by dipping the nares of each individual mice in viral medium daily. Endpoint titers from retrotracheal lavages and lung homogenates were taken at day 10. Data from n=3 cages. **b**. Mean ± SEM body weight of index and contact mice. **c**. Survival of index and contact mice. **d.** Viral burden in shedding samples analyzed plaque assay for infectious virus. Data shown as geometric mean (line) with geometric standard deviation (dotted lines). Individual values below the limit of detection were set to 5, corresponding to 1 log below the limit of detection. **e.** Viral burden in shedding samples, retrotracheal lavage, or lungs at day 10. **f.** 13-week-old K18-hACE2$^{+/-}$ mice were infected intranasally with a lethal dose (10,000 PFU) of SARS-CoV-2 WA-1 (index) and cohoused with uninfected littermates (contact) for 22 days at an index:contact ratio of 1:2 or 1:3. Negative control animals were inoculated with PBS, and positive control animals with a sub-lethal dose of 1,000 PFU. Seroconversion was determined by ELISA for Spike IgG. Data shown as mean ± SEM from animals in n=3 cages. **g.** Experimental overview for panels h-j. 4 to 7 days old K18-hACE2$^{+/-}$ pups were infected intranasally with either 1,500, 15,000 or 50,000 PFU of SARS-CoV-2 WA-1 for 4 days. Weight and survival were monitored daily. Viral shedding samples were collected by dipping the nares of each individual pup in viral medium daily. Data from at least n=3 mice per group. **h**. Mean ± SEM body weight. Dotted lines represent last day of survival of each group. **i**. Survival **j.** Viral burden in shedding samples analyzed by plaque assay for infectious virus. Data shown as as mean ± SEM. **k**. 4 to 7 days old K18-hACE2$^{+/-}$ pups were infected intranasally with either 15,000 PFU of SARS-CoV-2 WA-1 or heat-inactivated SARS-CoV-2 WA-1 for 4 days. Viral burden in daily shedding samples was evaluated by RT-qPCR. Data shown as individual values (symbols) and mean (lines) from at least n=4 individual mice per group.

efficiency of SARS-CoV-2 transmission in adult mice in our hands, we infected 13-week-old K18-hACE2 index mice intranasally, under anesthesia, with a lethal dose (10,000 PFU titered in VeroE6-TMPRESS2-T2A-ACE2 cells) of ancestral SARS-CoV-2 USA_WA-1/2020 (WA-1). Starting at the day of infection, we co-housed the infected index mice with naïve contacts at a ratio of 1 index to 2-3 contacts (**Supplemental Fig. 1a**). We monitored morbidity (weight loss) and mortality (humane endpoint) and collected longitudinal nasal shedding samples non-invasively and without anesthesia, by dipping the nares in viral media. Thus, we were able to leverage the kinetics of upper respiratory tract (URT) shedding in individual mice, longitudinally, as a measure of viral infection. In contrast to index mice, we did not observe morbidity or mortality in contact mice by the end of the experiment (10 days post index infection) (**Supplemental Fig. 1b, c**). Index mice shed infectious particles starting from day 1-6 post infection, with peak viral shedding at day 2 (**Supplemental Fig. 1d**). We detected infectious virus in URT shedding samples at any time point in only 1/9 (11% total) of the contact animals (**Supplemental Fig. 1d**). This was the same contact animal that still had infectious titers in the URT and the lung at 10 dpi (**Supplemental Fig. 1e**). By cage, this represented 0/3 (0%), 0/3 (0%), or 1/3 (33 %) transmission efficiency. In a parallel experiment, we determined transmission by contact seroconversion (**Supplemental Fig. 1f**). PBS-infected mice served as negative control, and mice infected at a sublethal dose (1,000 PFU) as a positive control for seroconversion. At the experimental endpoint of 22 days post index infection, we found that 1/5 (20%) of contact mice had seroconverted (**Supplemental Fig. 1f**). By cage, this represented 0/3 (0%), or 1/2 (50 %) transmission. We concluded that contact transmission of WA-1 in adult K18-hACE2 mice does occur, albeit at low efficiency and

with high cage-to-cage variability. Thus, like the influenza virus model of transmission, we next set out to establish SARS-CoV-2 infection in neonate mice.

We first performed a dose-response experiment to determine the minimum viral dose required to yield robust SARS-CoV-2 infection and shedding in neonates. We combined C57BL/6 K18-hACE2$^{+/+}$ males and C57BL/6 (hACE2$^{-/-}$) females to produce SARS-CoV-2 WA-1 permissive K18-hACE2$^{+/-}$ offspring. At 4-7 days of age, pups were infected intranasally with 3 µL of ancestral WA-1 without anesthesia. We used an escalating viral dose of 1,500, 15,000 or 50,000 PFU. We then monitored morbidity (lack of weight gain) and mortality (humane endpoint) and collected daily longitudinal nasal shedding samples by dipping the nares in collection media (**Supplemental Fig. 1g**). Pups infected with 1,500 PFU failed to gain further weight by day 3 post-infection (3 dpi), and they all succumbed to infection by 4 dpi. Pups infected with 15,000 or 50,000 PFU died at 3 dpi before detectable weight loss occurred (**Supplemental Fig. 1h, i**). Nasal shedding titers between pups infected with 1,500, 15,000 or 50,000 PFU were similar on 1 and 2 dpi, but became apparent on 3 dpi (**Supplemental Fig. 1j**): titers from pups infected with 1,500 PFU declined compared to 2 dpi, whereas titers from pups infected with 15,000 PFU remained at the same level as 2 dpi, and titers from pups infected with 50,000 PFU increased beyond that detected at 2 dpi. The detected shedding titer difference between the 1,500 and 50,000 PFU groups at 3 dpi was about 100-fold. This shows that an escalating input titer can modulate the dynamic of viral shedding in our model. As the lowest tested dose of 1,500 PFU yielded robust infection while leaving an additional day for transmission to occur before index mice succumb to infection, we used

1,500 PFU as the standardized inoculum in subsequent neonatal mouse infection experiments.

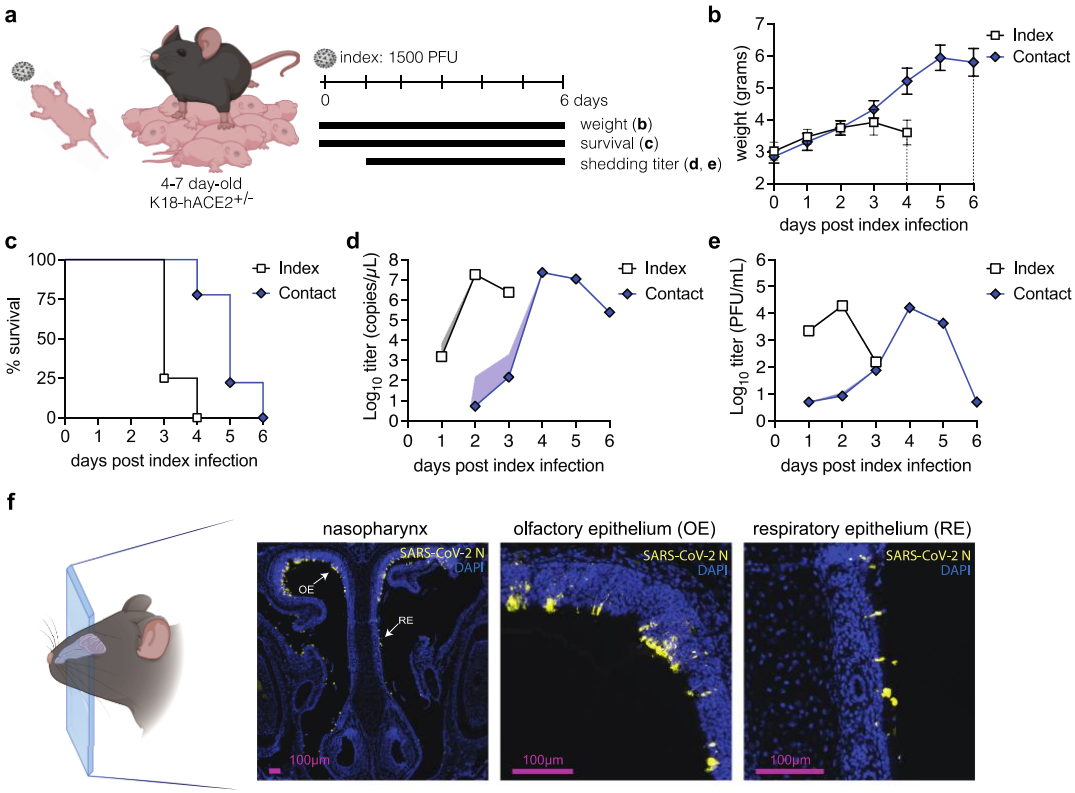

Figure 1. Establishment of a neonatal K18-hACE2 mouse transmission model using SARS-CoV-2 WA-1. a. Experimental overview for panels (b-e). 4 to 7 day old K18-hACE2$^{+/-}$ pups were infected intranasally with 1500 PFU of SARS-CoV-2 WA-1 (index) and cohoused with uninfected littermates (contact) for 6 days. Weight and survival were monitored daily. Viral shedding samples were collected by dipping the nares of each individual pup in viral medium daily. Data represents at least 2 independent repetitions. n = 4 - 6 contact mice per repetition. **b.** Mean ± SEM body weight of index and contact pups. Dotted lines represent last day of survival of each group. **c.** Survival of index and contact pups. **d.** Viral burden in shedding samples analyzed by RT-qPCR for SARS-CoV-2 RNA and **e.** by plaque assay for infectious virus. Data shown as geometric mean (line) with geometric standard deviation (dotted lines). Individual values below the limit of detection were set to 5, corresponding to 1 log below the limit of detection. **f.** Immunohistochemistry for SARS-CoV-2 N in 4-7 day old mice nasopharynx. Pups were infected intranasally with 1500 PFU of SARS-CoV-2 WA-1 and heads were fixed at 2 dpi, paraffin embedded, sectioned through the nasopharynx, and stained for SARS-CoV-2 N protein (yellow) and DAPI (blue) for nuclei. Arrows represent areas magnified in the adjacent panels. OE - olfactory epithelium, RE - respiratory epithelium

Next, we tested intra-litter transmission of WA-1 in neonatal mice. We infected 4–7-day old K18-hACE2$^{+/-}$ index mice with 1,500 PFU of WA-1 and placed them back with the (non-permissive) dam and their (permissive) naïve littermates at a ratio of 1 index to 4-6 contact mice (**Fig. 1a**). We first observed that both morbidity and mortality were offset in contact mice by 2-3 days compared to index mice (**Fig. 1b, c**), indicating successful transmission. In index mice, we detected SARS-CoV-2 RNA as early as 1 dpi, peaking at 2 dpi, whereas some contact pups began shedding viral RNA from 2 dpi, peaking at 4 dpi

(**Fig. 1d**). A parallel experiment with heat-inactivated SARS-CoV-2 showed that the viral genomes in shedding samples were due to active viral replication and not carryover from inocula (**Supplemental Fig. 1k**). Detecting SARS-CoV-2 RNA in contact mice was thus another indication of transmission. However, we stringently define transmission as the sustained detection of infectious viral particles in contact mice. Therefore, we determined viral titers in nasal shedding samples by plaque assay. Infectious particles from index mice (**Fig. 1e**) correlated with the onset and waning of RNA detection (**Fig. 1d**). Detection of infectious particles in contact pups confirmed SARS-CoV-2 transmission. Infectious particles in contacts peaked on day 4 and decreased by days 5 and 6, similar to SARS-CoV-2 RNA trends. Of note, all contact pups shed infectious particles by day 4, representing 16/16 (100%) transmission of WA-1 in our model.

Detection of infectious particles in shedding samples of K18-hACE2 neonatal mice suggested robust viral infection in the URT. To determine the sites of infection within the URT in spatial granularity, we performed immunohistochemistry (IHC) on the nasopharynx of index pups. Heads of neonatal mice were harvested at their peak of viral shedding (2 dpi), sectioned through the nasopharynx, and stained for SARS-CoV-2 N protein. We detected SARS-CoV-2-positive cells in the upper olfactory and respiratory epithelium lining, demonstrating replication of SARS-CoV-2 WA-1 in cells of the URT (**Fig. 1f**). Taken together, these results establish and validate a tractable neonatal K18-hACE2 mouse model for the transmission of SARS-CoV-2.

SARS-CoV-2 variants of concern display distinct replication dynamics and tropism in neonatal index mice

High transmissibility of SARS-CoV-2 Alpha and Delta variants has been proposed to be driven by efficient URT replication and shedding[30,31]. This is in contrast to the influenza virus literature, where URT replication is not correlated with aerosol generation or transmission in humans[32]. Using the neonate mouse model, we experimentally recapitulated that influenza virus transmission efficiency does not correlate with URT titers, but rather with the amount of exhaled virus in shed secretions[18]. Others have shown that influenza virus transmission is dependent on both the timing to and magnitude of peak shedding[33,34]. Similar observations were noted for SARS CoV-2 in Syrian hamsters where oral virus titers from swabs was a poor proxy for airborne shedding, yet peak airborne virus shed into the environment correlated with transmission[35].

To identify the index correlates of SARS-CoV-2 transmission in our model, we characterized viral loads in various respiratory compartments: lower respiratory tract (lung homogenates), URT (retro tracheal lavages), or shed secretions (expelled virus). We began by evaluating the dynamics of viral replication within these compartments for the ancestral WA-1 virus. 4–7-day old K18-hACE2$^{+/-}$ pups were infected with 1,500 PFU of WA-1 and measured infectious particle load in the respective sample type at 1, 2 and 3 dpi (**Fig. 2a, b**, **Supplemental Fig. 2a**). At 1 dpi, expelled and URT titers were both higher than lung titers, albeit not statistically significant. At 2 dpi, expelled, URT, and lung titers were similar in titer to each other. At 3 dpi, shedding titers declined, while lung titers increased, resulting in lung titers that were significantly higher than shedding titers. This

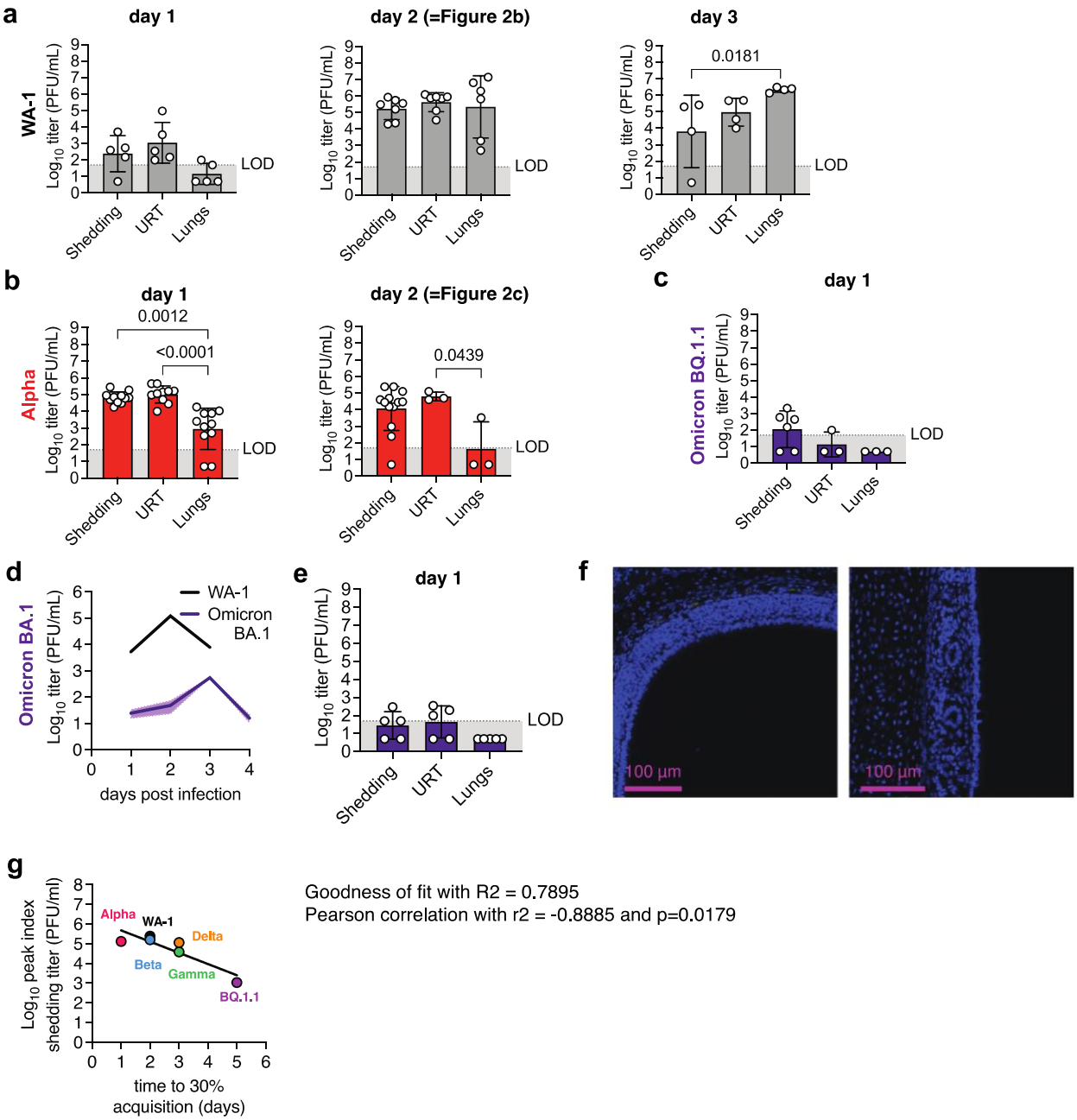

Supplemental Figure 2, related to Figures 2 and 3: SARS-CoV-2 replication dynamics and tropism in index mice. a.-c. 4-7 day old K18-hACE2$^{+/-}$ pups were infected intranasally with 1500 PFU of SARS-CoV-2 WA-1 (**a**), Alpha (**b**), or Omicron BQ.1.1 (**c**). At indicated days, we collected shedding titers by dipping the nares into collection medium and sacrificed some pups to collect retrotracheal lavages and lungs to determine viral infectious virus titers. Data of Shedding, URT and Lung titers are shown as symbols for individual pups; bars and error bars represent the geometric mean and geometric standard deviation, respectively. Data from at least n=3 pups per group. LOD - limit of detection. Individual values below the LOD were set to 5, corresponding to 1 log below the LOD. p-values were determined by Kruskal-Wallis test. Only significant values are presented. Day 2 panels are identical with those in Figure 2 a and c, respectively, and shown again here for easea of sice-by-side comparison. **d.-f.** 4-7 day old K18-hACE2$^{+/-}$ pups were infected intranasally with 1500 PFU of SARS-CoV-2 Omicron BA.1. **d.** Viral shedding samples were collected daily by dipping the nares of each individual pup in viral medium. Daily shedding data is shown as geometric mean (line) with geometric standard deviation (dotted lines). Day 0, inoculum. Data from at least 2 independent repetitions with n = 6 - 15 pups per group. **e.** At 1 dpi, we sacrificed some pups to collect retrotracheal lavages and lungs to determine viral infectious virus titers. Data of Shedding, URT and Lung titers are shown as symbols for individual pups; bars and error bars represent the geometric mean and geometric standard deviation, respectively. Data from at least n=5 pups per group. LOD - limit of detection. Individual values below the LOD were set to 5, corresponding to 1 log below the LOD. p-values were determined by Kruskal-Wallis test. Only significant values are presented. **f.** Immunohistochemistry for SARS-CoV-2 N at 1 dpi with Omicron BA.1 in neonatal mice nasopharynx. Heads were paraffin embedded, sectioned through the nasopharynx, and stained for SARS-CoV-2 N protein (yellow) and DAPI (blue) for nuclei. **g.** Peak index shedding titers (Fig 2) shown over time to 30 % acquisition in contacts (Fig 3). Best fit linear regression curves were fitted on data and goodness of fit (R2), Pearson correlation (r2) and significance (p value) was calculated using GraphPad Prism 9.5 software.

223

suggests that in our model, SARS-CoV-2 WA-1 infection administered in low volume intranasally without anesthesia progresses from the URT to the lungs over time.

Next, we compared URT shedding dynamics of ancestral virus and variants. We first generated clonal (plaque-purified), sucrose-purified, and deep-sequenced viral working stocks. This rigorous quality-control pipeline ensures the identity of VOCs (i.e., the presence of variant-defining mutations) and their integrity (the lack of tissue culture-induced mutations). We then infected K18-hACE2$^{+/-}$ pups with 1,500 PFU of either Alpha (B.1.1.7), Beta (B.1.1.351), Gamma (P.1), Delta (B.1.617.2), Omicron BA.1, or Omicron BQ.1.1. We first determined the dynamics of infectious virus shedding for each isolate from 1-4 dpi or until the pups succumbed to infection (**Fig. 2a, Supplemental Fig. 3**). Shedding from mice infected with ancestral WA-1 peaked at 2 dpi before decreasing by 3 dpi (**Fig. 2b**). In contrast to WA-1, shedding from mice infected with Alpha peaked earlier, at 1 dpi, and steeply decreased by 2 dpi (**Fig. 2c**). Shedding from mice infected with Beta also peaked at 1, but, in contrast to Alpha, remained at the same level on 2 dpi before declining on 3 dpi, resulting in a titer similar to WA-1-infected pups (**Fig. 2d**). Shedding from mice infected with Gamma, and Delta had a slope similar to WA-1, with a peak at 2 dpi, before decreasing by 3 dpi (**Fig. 2e, f**). Shedding titers from Gamma-infected pups were on average lower than those from WA-1-infected pups, albeit not statistically significant (**Fig. 2e**). Mice infected with Omicron isolates BA.1 or BQ1.1 shed overall low levels of virus, with most replicates below the detection limit (**Fig. 2g, Supplemental Fig. 2d**). However, these two Omicron variants differ with respect to shedding kinetics: BQ.1.1 shedding peaked at 1 dpi versus BA.1 at 3 dpi (**Fig. 2g**,

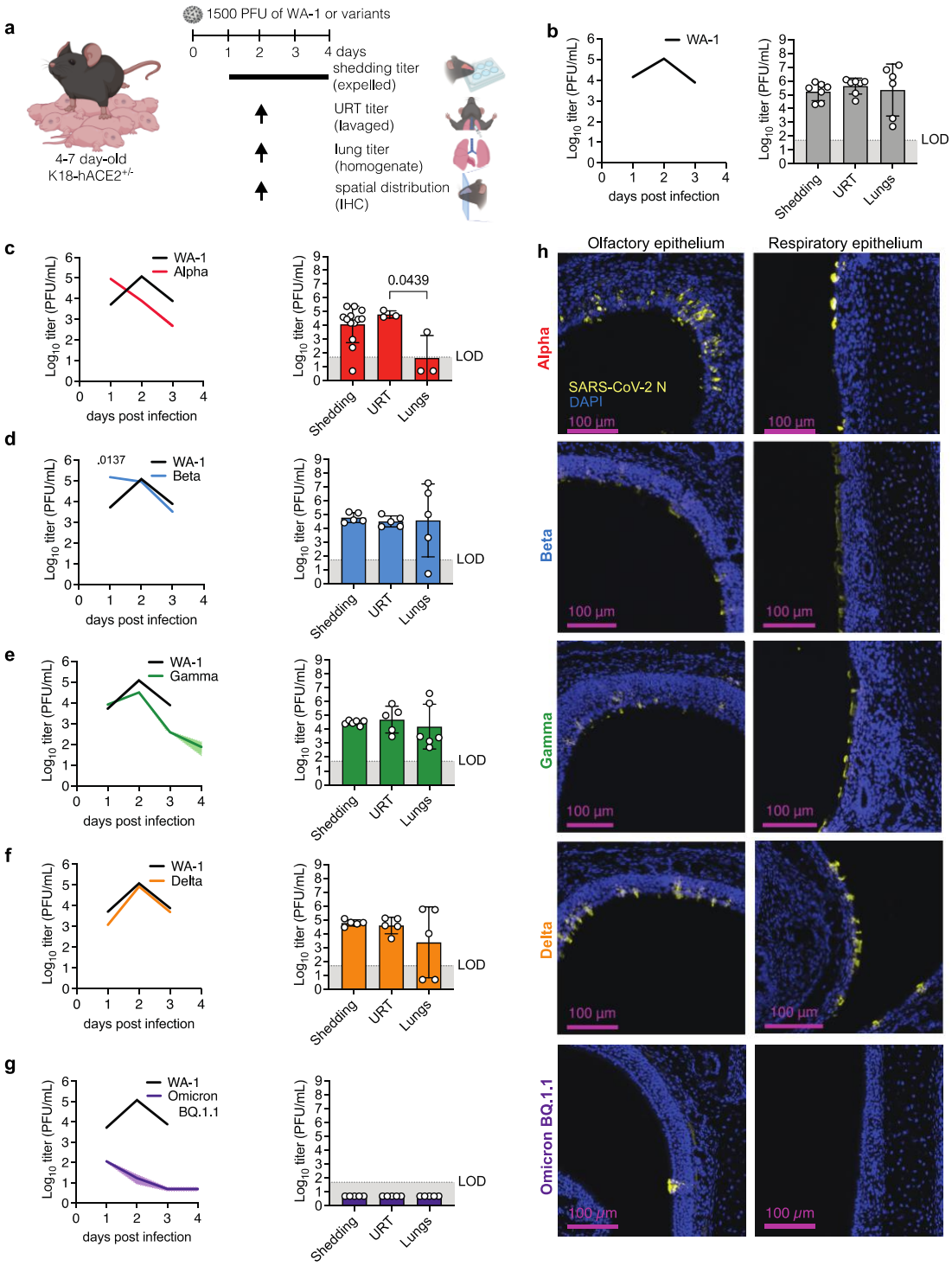

Figure 2: SARS-CoV-2 variant replication dynamics and tropism in index mice. a. Experimental overview. 4-7 day old K18-hACE2$^{+/-}$ pups were infected intranasally with 1500 PFU of SARS-CoV-2 WA-1 or variants of concern. Viral shedding samples were collected daily by dipping the nares of each individual pup in viral medium. At 2 dpi, we sacrificed some pups to collect retrotracheal lavages and lungs to determine viral infectious virus titers, and to fix heads for immunohistochemistry of the nasopharynx. **b-g.** Viral burden in daily shedding samples (left panels) and viral burden at 2 dpi, URT and Lung samples (right panels). Daily shedding data is shown as geometric mean (line) with geometric standard deviation (dotted lines). Data from at least 2 independent repetitions with n = 6 - 15 pups per group. Peak day data of Shedding, URT and Lung titers are shown as symbols for individual pups; bars and error bars represent the geometric mean and geometric standard deviation, respectively. Data from at least n=5 pups per group. LOD - limit of detection. Individual values below the LOD were set to 5, corresponding to 1 log below the LOD. p-values were determined by Kruskal-Wallis test. Only significant values are presented. **i**. Immunohistochemistry for SARS-CoV-2 N at 2 dpi in neonatal mice nasopharynx. Heads were paraffin embedded, sectioned through the nasopharynx, and stained for SARS-CoV-2 N protein (yellow) and DAPI (blue) for nuclei.

246

Supplemental Fig. 2d). Thus, our model is able to capture the unique kinetics of SARS-CoV-2 variant URT shedding from infected pups.

We next compared the sites of viral replication for each variant and found the distribution of viral load in different sample types to be distinct for specific viruses. For Alpha, shedding and URT titers at 2 dpi were comparable in magnitude to 2 dpi WA-1 (**Fig. 2b, c**), but lung titers were trending lower (**Fig. 2c**). To determine whether these lower lung titers were a consequence of Alpha's earlier onset and waning of replication and shedding, we assayed Alpha viral loads in the three compartments also at Alpha's peak day of shedding, 1 dpi (**Supplemental Fig. 2b**, left panel). Again, we found significantly higher titers in the shedding and URT samples than in the lungs, suggesting that, in our model, both on 1 and 2 dpi, Alpha replicates better in the URT. For Beta, Gamma, and Delta we found no significant differences in titers between shed virus, URT, and lungs, suggesting equal ability to infect and replicate in both the URT and the lower respiratory tract and to be shed from the URT (**Fig. 2 d-f**). Indeed, IHC of the URT region confirmed that WA-1, Alpha, Beta, Gamma, and Delta infect the URT efficiently (**Fig. 2h**). In contrast, BQ1.1 titers in URT and lungs at 2 dpi were undetectable (**Fig. 2g**), and IHC did not reveal Omicron BQ.1.1-infected cells in the URT epithelium (**Fig. 2h**). To determine whether these undetectable titers were a consequence of BQ1.1's earlier onset and waning of replication and shedding, we assayed Omicron BQ.1.1 viral loads in the three compartments also at its peak day of shedding, 1 dpi. We found that average titers were still low in all three compartments, and that some samples were above the limit of detection in shedding and URT samples (**Supplemental Fig. 2c**). These results were similar to 1 dpi data obtained for Omicron BA.1 (**Supplemental Fig. 2e, f**). No infectious

Omicron particles were detected in the lungs for either Omicron sub-variant, suggesting that Omicron does not replicate efficiently in neonatal K18-hACE2 mice (**Fig. 2g, Supplemental Fig. 2e**). Our results are in line with findings from others, showing that Omicron variants are attenuated in hamsters and mice, despite the presence of its receptor hACE2 in the K18 model[25,36,37].

Interestingly, viral loads in shedding samples were similar to those from their respective retro tracheal lavage samples for all viral isolates, showing that, in our model, SARS-CoV-2 viruses assayed do not display a defect in viral expulsion, and thus, URT shedding can be used as a proxy for SARS-CoV-2 URT replication.

Taken together, our results demonstrate that, except for Omicron variants, our model allows for efficient replication and shedding of SARS-CoV-2 variants at comparable levels to the ancestral WA-1. Temporal shedding kinetics differ between variants and permits this model to be used as a tool to understand the mechanisms of variant SARS-CoV-2 transmission.

Neonatal mouse model reveals dynamics in SARS-CoV-2 variant transmission

We next utilized our panel of SARS-CoV-2 variants ranging from early to current pandemic isolates to test transmission. 4-7-day-old index K18-hACE2$^{+/-}$ mice were infected with either ancestral SARS-CoV-2 WA-1, Alpha, Beta, Gamma, Delta, Omicron BA.1 or Omicron BQ.1.1 and cohoused with naïve neonatal mice at a 1:6-9 ratio. WA-1, Alpha-, Beta-, and Delta-infected index mice all succumbed to infection by 3 dpi (**Supplemental Fig. 3a-c, e**). Gamma-infected index mice succumbed by 4 dpi (**Supplemental Fig. 3d**). For Delta- and Omicron BA.1-infected index mice, morbidity

(lack of weight gain) and mortality were delayed, and for Omicron BQ.1.1-infected index mice, we did not detect substantial morbidity and incomplete mortality of index mice (**Supplemental Fig. 3e-g**). Transmission events occurring at late time points, after the death of index pups, may stem either from late onset of contact shedding or from sequential transmission between contacts. Except for the two Omicron variants, some, or all contact mice in cages with other variants succumbed to infection by 7 dpi (**Supplemental Fig. 3**).

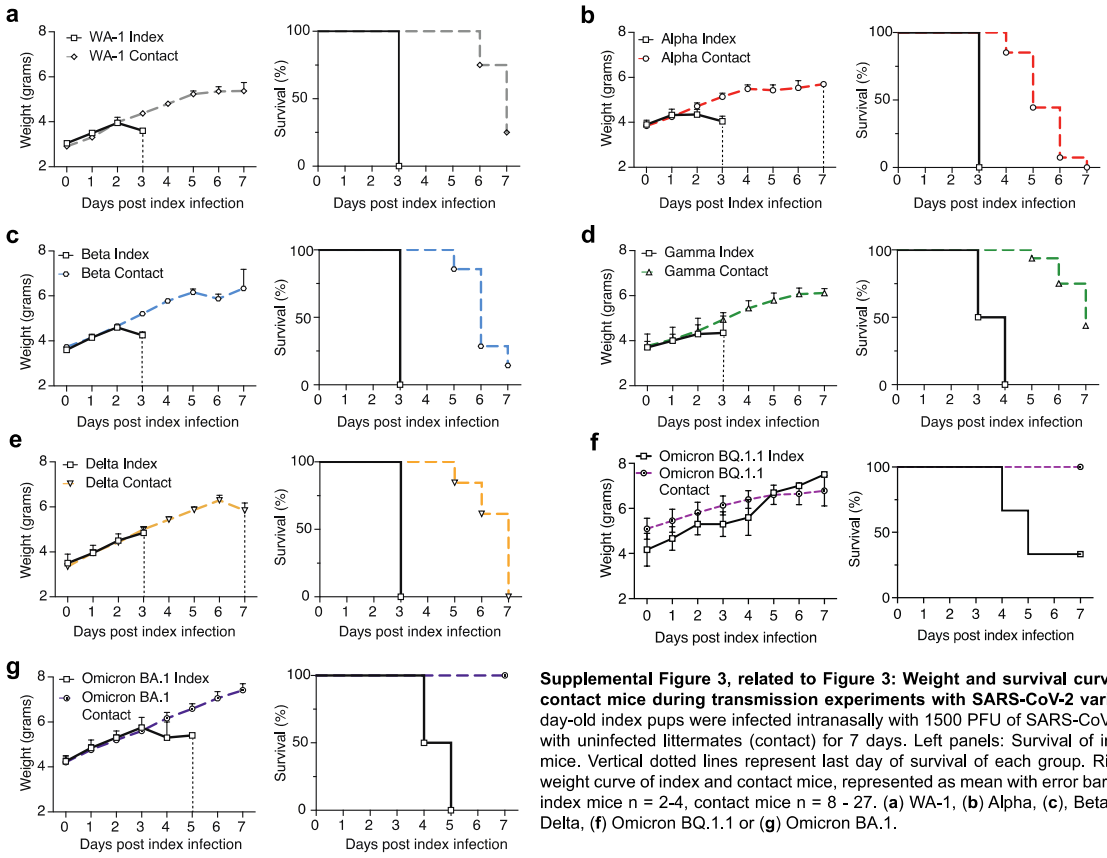

Supplemental Figure 3, related to Figure 3: Weight and survival curves of index and contact mice during transmission experiments with SARS-CoV-2 variants. a-g. 4 to 7 day-old index pups were infected intranasally with 1500 PFU of SARS-CoV-2 and cohoused with uninfected littermates (contact) for 7 days. Left panels: Survival of index and contact mice. Vertical dotted lines represent last day of survival of each group. Right panels: body weight curve of index and contact mice, represented as mean with error bars indicating SEM. index mice n = 2-4, contact mice n = 8 - 27. (**a**) WA-1, (**b**) Alpha, (**c**), Beta, (**d**) Gamma, (**e**) Delta, (**f**) Omicron BQ.1.1 or (**g**) Omicron BA.1.

We next investigated the dynamics of transmission using two non-redundant readouts from contact pups: 1. Timing of viral acquisition by contacts: We quantify virus acquisition by contact pups as “transmission events” when virus is detected at least twice in shedding samples (**Fig. 3**). The first day of viral shedding from each contact (“infectious

virus-positive”) is counted as the onset of acquisition. This lets us evaluate viral acquisition as a function of time and compare the kinetics of acquisition between variants. This readout does, however, not depict the amplitude of contact infection. 2. Detection of viral titers from URT shedding of contact animals: This measure allows the detection of subtle variations in the level of contact shedding. The differences in shedding amplitude observed in our experiments may stem from the variations in shedding by the index mice (i.e., infectious dose and timing of transmission by the index), and/or differences in the viral replicative fitness in contacts. Changes in contact shedding titers may matter in sequential transmission experiments, where contacts become index for naïve individuals. For WA-1 and Alpha, 100 % transmission was reached by 3 or 4 dpi, respectively, with slopes that were not significantly different (**Fig. 3a**, left panel). Both ancestral WA-1 and Alpha infectious particles were detected in some contact mice as early as 1 dpi, and Alpha’s were significantly higher than WA-1’s on 3 dpi, suggesting a slight transmission advantage by Alpha. Alpha contact shedding titers peaked at 4 dpi, and faded earlier than WA-1, starting at 4 dpi, (**Fig. 3a,** right panel), which is in line with the early drop of shedding titers previously observed in Alpha index mice (**Fig. 2c**). In contrast to Alpha, Beta contact mice displayed significantly delayed acquisition compared WA-1 (**Fig. 3b**, left panel), but reached similar peak contact titers (**Fig. 3b**, right panel). Gamma contact mice showed significantly delayed acquisition compared to WA-1 (**Fig. 3c**, left panel), and achieved a 73% transmission overall. Gamma contact mice also had an overall lower viral load, although kinetics to and from peak titer was similar to that of WA-1 (**Fig. 3c,** right panel). Like Gamma, Delta contact mice significantly lagged WA-1 contact mice regarding acquisition (**Fig. 3d**, left panel), and Delta contacts peak infectious virus levels were

similar to WA-1 (**Fig. 3d**, right panel). Delta-infected contacts continued shedding infectious particles until the end of the experiment at 7 dpi (**Fig. 3d**, right panel). Omicron BA.1 contact mice did not acquire infection in our model or shed infectious virus (**Fig. 3e)**, which is in line with other reports showing that Omicron BA.1 is attenuated, and airborne transmission is reduced in rodents[25,36-38]. Interestingly, and in contrast to BA.1, Omicron BQ.1.1 contact mice achieved 33.3% transmission in our model (**Fig. 3f**, left panel). BQ.1.1. index shed with exceptionally low viral titers (**Fig. 2g**) which corresponded with a lower transmission rate and low contact shedding (**Fig. 3f**, right panel). The transmission difference between BA.1 and BQ.1.1 was surprising given that peak shedding titers of both Omicron subvariants in index animals were equally low (**Fig. 2g**, **Supplemental Fig. 2c**). It is possible that the timing of peak shedding (1 dpi for BQ.1.1 vs 3 dpi for BA.1) is the critical determinant for Omicron transmission in our model. Overall, our data shows that the magnitude of index shedding corresponds with the success of transmission to contacts (**Supplemental Fig. 2g**).

Next, we characterized the URT inflammatory repertoire of index mice after viral challenge in our model. An antiviral/inflammatory response to infection is expected to attenuate the virus within the host, causing reduced transmission[8,39]. However, increased inflammation may also induce URT secretions that help expel the virus into the environment, which may favor transmission[21,23]. We analyzed the cytokines present in URT shedding samples of index mice by multiplex ELISA at 6, 24 and 48 h, using heat-inactivated (HI) SARS-CoV-2 WA-1 or poly (I:C) as controls. We detected the presence of multiple cytokines in poly(I:C)-treated mice at the 48 h timepoint, albeit at levels that were lower than in WA-1-infected mice (**Supplemental Fig. 4a**). HI WA-1 failed to induce

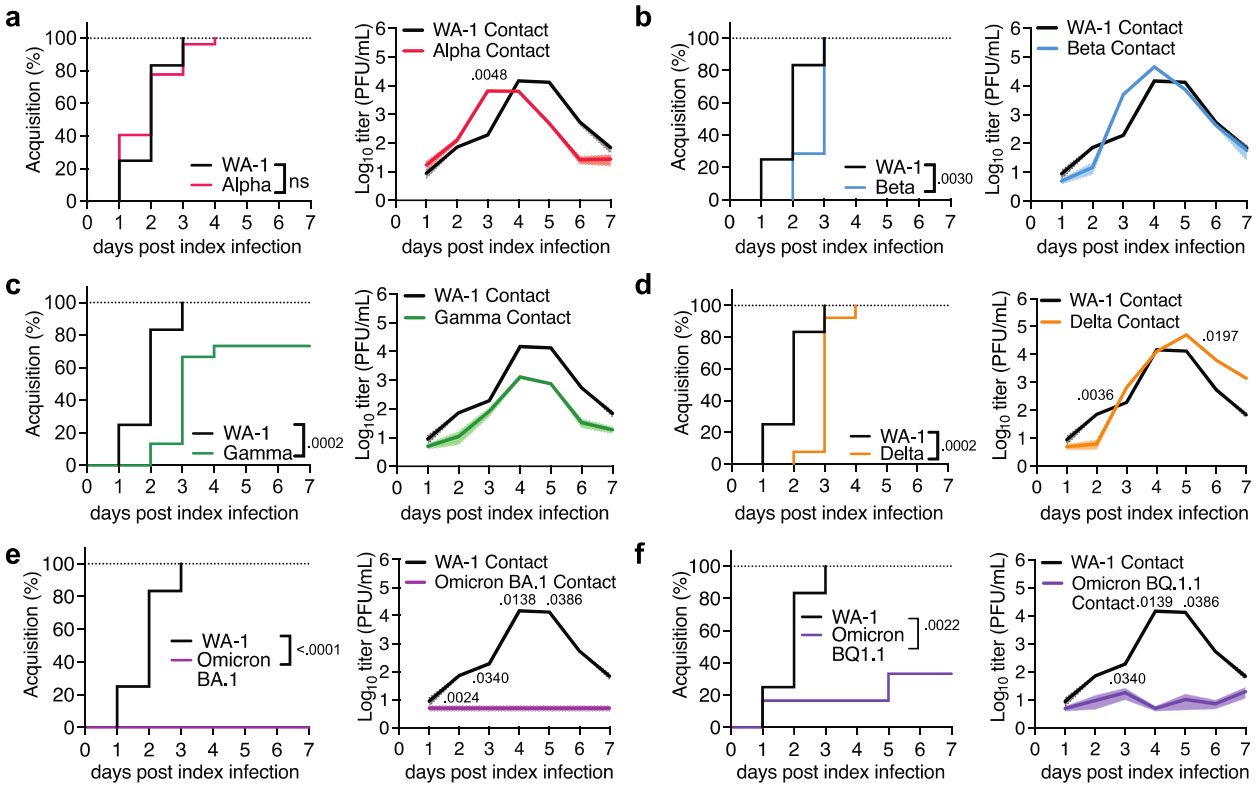

Figure 3: SARS-CoV-2 variant transmission in neonatal mice. 4 to 7 day old K18-hACE2$^{+/-}$ pups were infected intranasally with 1500 PFU of SARS-CoV-2 WA-1 (index) and cohoused with uninfected littermates (contact) for 7 days at a ratio of 1 index to 6-9 contacts. Viral shedding samples were collected by dipping the nares of each individual contact pup in viral medium daily. Data represents at least 2 independent repetitions. n = 4 - 6 contact pups per repetition. **a.-e.** Left panels: % Acquisition shown in inverted Kaplan-Meier plots. Acquisition events were scored as at least two days of infectious viral titer in shedding samples. The onset of acquisition was scored as the first day of infectious virus detection. p-values by Mantel-Cox Log-rank test. Right panels: viral burden in contact shedding samples. Data shown as geometric mean (line) with geometric standard deviation (shaded areas). Individual values below the limit of detection were set to 5, corresponding to 1 log below the limit of detection. **a.-e.** right panels: viral burden in contact shedding samples analyzed by plaque assay for infectious virus. Data shown as geometric mean (line) with geometric standard deviation (shaded areas). Individual values below the limit of detection were set to 5, corresponding to 1 log below the limit of detection. **a.**, WA-1 vs Alpha, **b.** WA-1 vs Beta, **c.** WA-1 vs Gamma, **d.** WA-1 vs Delta, **e.** WA-1 vs Omicron BA.1, **f.** WA-1 vs Omicron BQ1.1.

measurable inflammation across timepoints, whereas we detected increased cytokine levels in samples from WA-1-infected mice by 48 h (**Supplemental Fig. 4a**). This suggests that our purified viral stocks do not contain exogenous inflammatory material, that active WA-1 replication is required to drive inflammation in our model, and that the 48 h timepoint is optimal to measure the cytokine profile in URT shedding samples.

To explore a potential association between index URT inflammation and transmission, we measured cytokines in shedding samples of index mice infected with either ancestral SARS-CoV-2 WA-1 or variants Alpha, Beta, Gamma, Delta, Omicron

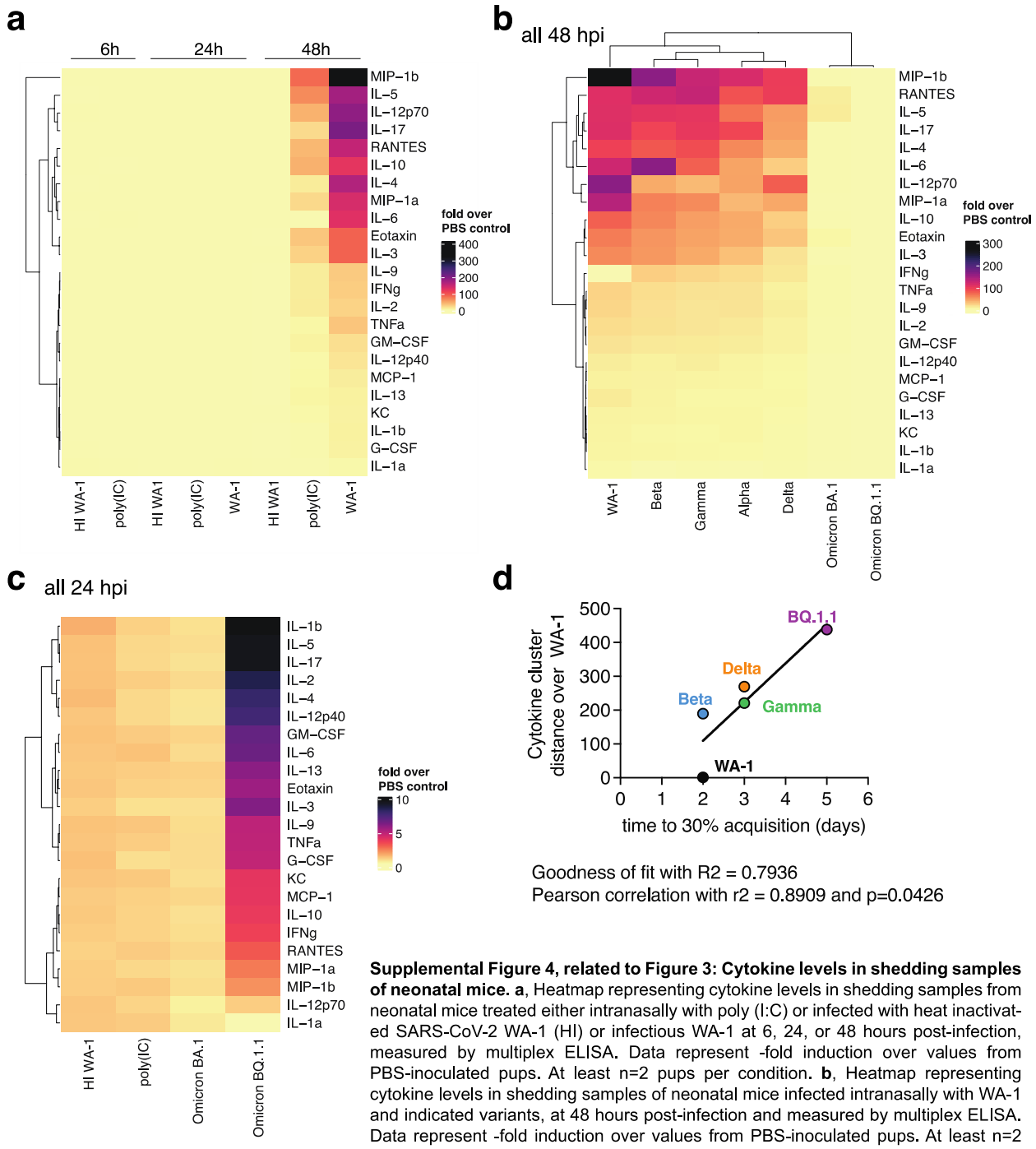

Supplemental Figure 4, related to Figure 3: Cytokine levels in shedding samples of neonatal mice. a, Heatmap representing cytokine levels in shedding samples from neonatal mice treated either intranasally with poly (I:C) or infected with heat inactivated SARS-CoV-2 WA-1 (HI) or infectious WA-1 at 6, 24, or 48 hours post-infection, measured by multiplex ELISA. Data represent -fold induction over values from PBS-inoculated pups. At least n=2 pups per condition. **b**, Heatmap representing cytokine levels in shedding samples of neonatal mice infected intranasally with WA-1 and indicated variants, at 48 hours post-infection and measured by multiplex ELISA. Data represent -fold induction over values from PBS-inoculated pups. At least n=2 pups per condition. **c.** Heatmap representing cytokine levels in shedding samples of neonatal mice infected with heat inactivated SARS-CoV-2 WA-1 (HI) or infectious SARS-CoV-2 Omicron BA.1 or BQ.1.1 variants, at 24 hours post-infection and measured by multiplex ELISA. Data represent -fold induction over values from PBS-inoculated pups. At least n=2 pups per condition. **d.** Cytokine cluster distance (panel b) shown over time to 30% acquisition in contacts (Fig. 3). Best fit linear regression curves were fitted on data and goodness of fit (R2), Pearson correlation (r2) and significance (p value) was calculated using GraphPad Prism 9.5 software. Alpha was omitted from the analysis.

360

BA.1 and Omicron BQ.1.1 at 48 hpi. Comparable infectious viral shedding titers at this time point for most variants, between 10^4 and 10^5 PFU/mL (Fig. **2**), allowed for qualitative comparison of cytokine signatures between these equally replicating viruses. Both Omicron variants had much lower viral shedding titers at 48 hpi (10^1 PFU/mL, **Fig 2g**), and accordingly, the cytokine signatures for both Omicron variants at 48 hpi were quiet (**Supplemental Fig. 4b**). Notably, at 24 hpi, which is the peak time of shedding for BQ.1.1, we detected increased cytokine levels in BQ.1.1-infected index (**Fig. 2g, Extended Data 4c**), but found no such increase in BA.1-infected mice, where shedding peaks later, at 72 hpi (**Supplemental Fig. 2d, Supplemental Fig. 4c**). For equally replicating viruses (WA-1, Alpha, Beta, Gamma, and Delta) we found that the cytokine signature upon ancestral WA-1 infection was the most different from signatures upon infection with variants (**Supplemental Fig. 4b**). Gamma and Alpha signatures clustered together, and so did Alpha and Delta signatures, respectively. The set of key upregulated cytokines was similar between equally replicating viruses (**Supplemental Fig. 4b,** upper left quadrant), but the amplitude of upregulation differed between viruses. Notably, cytokine cluster distance by the different viruses correlated with their respective transmission efficiency (Supplemental Fig. 4d), except Alpha. Further studies are needed to decipher whether any and if yes, which specific URT cytokines induced by index pups contribute to transmission (**Supplemental Fig. 4b** and **Fig. 3**). Our model and the availability of transgenic mice with interruptions in key cytokine pathways uniquely enables us to perform these future studies.

Taken together, our results show that our neonatal mouse model can characterize differences in transmission dynamics inherent to SARS-CoV-2 variants. Our daily method

of viral sampling enables tracking viral replication in individual index and contact mice over time, providing granularity in transmission parameters, including the association of variant-specific cytokine signatures and transmission.

Accessory proteins ORF6 and ORF8 play a role in successful SARS-CoV-2 transmission

In addition to mutations in spike, several SARS-CoV-2 variants display mutations in accessory genes, such as *ORF3*, *ORF6*, *ORF7*, and *ORF8*, which have been implicated in the interference of immune signaling or direct host effector counteraction[9,11,13,40-44]. The selective advantage of changes in these accessory proteins, if any, remains undefined, particularly regarding transmission. We thus aimed to determine how the lack of specific accessory proteins impacts SARS-CoV-2 transmission in our model, and focused on two accessory proteins: ORF8, because it has mutations defining the Alpha, Gamma, and Delta variants, and, ORF6, which lacks mutations in the variants utilized in this study but is mutated in some Omicron variants (i.e. BA.2, BA.4), in addition to being one of the best-characterized SARS-CoV-2 accessory proteins[4,42-44]. Both of these recombinant viruses have been characterized in cultured cells and in adult K18-hACE2 mice[45], revealing reduced viral titers *in vitro*, but similar lung titers *in vivo*. Interestingly, the virus lacking ORF8 displayed increased lung pathology score[45], which may suggest an increased inflammatory process is induced by this virus.

We infected K18-hACE2$^{+/-}$ neonatal mice with 1500 PFU of recombinant SARS-CoV-2 WA-1 (rWA-1), recombinant SARS-CoV-2 lacking ORF6 (ΔORF6), or recombinant SARS-CoV-2 lacking ORF8 (ΔORF8). Similar to our previous observations with the

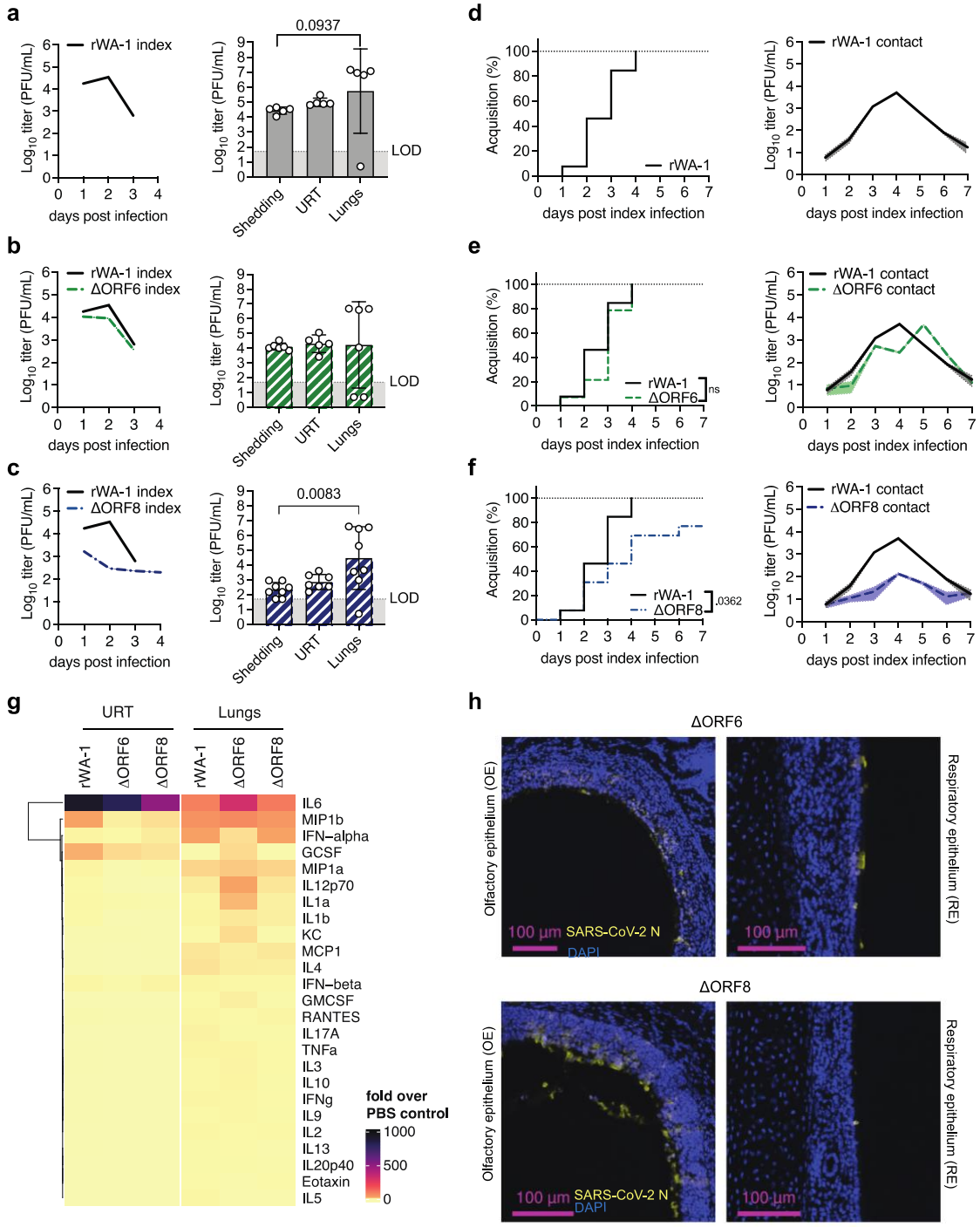

Figure 4. Recombinant SARS-CoV-2 ΔORF6 and ΔORF8 replication dynamics, tropism, transmission, and cytokine profiles. 4 to 7 day old K18-hACE2$^{+/-}$ pups were infected intranasally with 1500 PFU of (**a**) recombinant WA-1 (rWA-1), (**b**) rWA-1 lacking ORF6 (ΔORF6) or (**c**) rWA-1 lacking ORF8 (ΔORF8). These index pups were cohoused with uninfected littermates (contact) for 7 days at a ratio of 1 index to 6-9 contacts. Viral shedding samples were collected daily. At peak 2 dpi, we sacrificed some index pups to collect retrotracheal lavages and lungs to determine viral infectious virus titers. **a-c** Index mice. Left panels: viral burden in daily index shedding samples. Data is shown as geometric mean (line) with geometric standard deviation (dotted lines). Right panels: 2 dpi viral burden in index Shedding, URT and Lung samples. Data shown as symbols for individual pups; bars and error bars represent the geometric mean and geometric standard deviation, respectively. Data from at least n=5 pups per group. LOD - limit of detection. Individual values below the LOD were set to 5, corresponding to 1 log below the LOD. p-values were determined by Kruskal-Wallis test. Only significant values are presented. **d-f** Contact mice. Left panels: % Acquisition shown in inverted Kaplan-Meier plots. Acquisition events were scored as at least two days of infectious viral titer in shedding samples. The onset of acquisition was scored as the first day of infectious virus detection. p-values by Mantel-Cox Log-rank test. Right panels: viral burden in contact shedding samples. Data shown as geometric mean (line) with geometric standard deviation (shaded areas). Individual values below the limit of detection were set to 5, corresponding to 1 log below the limit of detection. **g.** Heatmap representing cytokine levels in shedding samples of neonatal mice infected intranasally with rWA-1, ΔORF6 or ΔORF8, at 48 hours post-infection and measured by multiplex ELISA. Data represent -fold induction over values from PBS-inoculated pups. At least n=3 pups per condition. URT = upper respiratory tract. **h.** Immunohistochemistry for SARS-CoV-2 N in neonatal mice nasopharynx infected with either ΔORF6 or ΔORF8, at 48 hours post-infection.

407

clinical WA-1 isolate (**Fig. 2b**), shedding titers from rWA-1 index mice peaked at 2 dpi and decreased by 3 dpi (**Fig. 4a,** left panel). Index shedding from ΔORF6 infected mice was similar to rWA-1 in kinetics, with a trend of lower magnitude (5-fold at 2 dpi, **Fig 4b,** left panel). Index mice infected with ΔORF8 consistently shed up to 100-fold less virus than mice infected with rWA-1 (**Fig. 4c,** left panel) and survived 1 day longer than rWA-1 infected index (**Supplemental Fig. 5a-c**), hence still shedding at 4 dpi. Next, we analyzed virus replication in shedding samples (expelled virus), URT lavages (URT replication), and lungs (lower respiratory tract replication) of index mice. Like the WA-1 isolate, we observed much higher rWA-1 titers in lungs than in the URT and shedding samples (**Fig. 4a**, right panel). For ΔORF6, we obtained similar titers in all three sample types, $1x10^4$ PFU/mL on average, although there was a broad distribution with some pups displaying higher viral titers in the lung than in shedding or URT samples (**Fig. 4b,** right panel). We concluded that, in our model, the lack of ORF6 did not significantly attenuate viral replication, shedding, or significantly change tissue tropism with respect to parental rWA-1. This was different for ORF8. ΔORF8 shedding and URT titers were lower than for rWA-1 or ΔORF6 (**Fig. 4c,** left panel). Surprisingly, viral burden in the lungs was comparable to those of rWA-1 and WA-1 ΔORF6. This was similar to previous findings in adult mice, where the lack of ORF8 did not alter lung titers[41,45]. Thus, the lack of ORF8 seems to significantly reduce ΔORF8's ability to robustly replicate specifically in the URT.

We next performed transmission experiments with the three recombinant viruses. Like the WA-1 isolate, rWA-1 acquisition by contacts occurred at 1 dpi, was complete by 4 dpi, and contact shedding titers decreased from 4 dpi onwards (**Fig. 4d**). ΔORF6 was similar to parental rWA-1 in both contact shedding onset, dynamics, and acquisition (**Fig.**

4e). Together, these results suggest that the lack of ORF6 does not significantly attenuate transmission in our model. Onset of acquisition for ΔORF8 was similar to rWA-1 and ΔORF6, 1 dpi, but in contrast to the other two recombinant viruses, the slope of acquisition was slower, and transmission was 76% (**Fig. 4f**). We hypothesize that this reduction in transmission efficiency is a consequence of the lower shedding titers by the index mice.

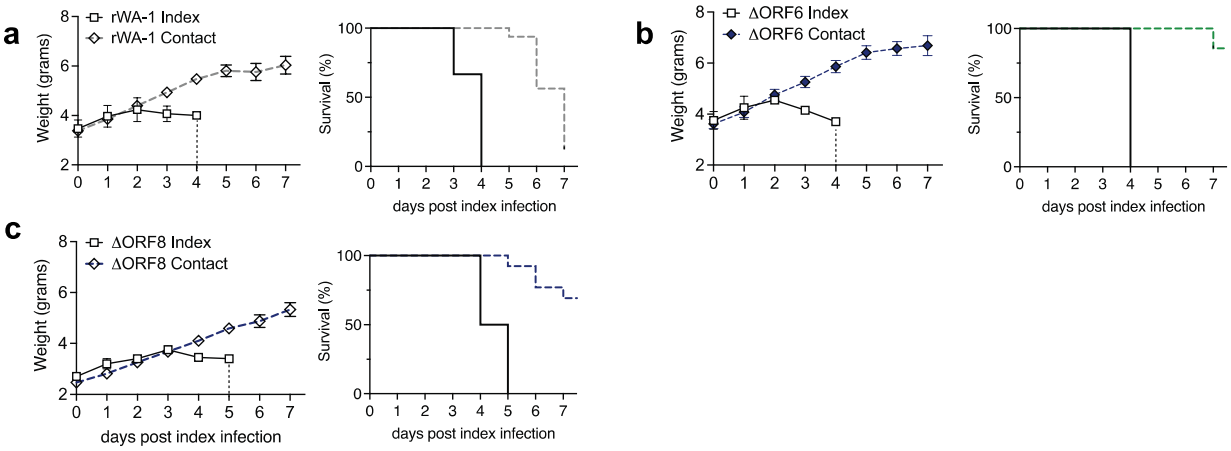

Supplemental Figure 5, related to Figure 4: Morbidity, mortality, and sites of upper respiratory viral replication for ΔORF6 and ΔORF8-infected neonatal mice. a-c, 4-7 day-old index pups were infected intranasally with 1500 PFU of indicated recombinant SARS-CoV-2 and cohoused with uninfected littermates (contact) for 7 days. Data corresponding to Figure 4. Left panels: Survival of index and contact mice. Vertical dotted lines represent the last day of survival of each group**.** Right panels: body weight curves of index and contact mice, represented as mean with error bars indicating SEM. Index mice n=2-4, contact mice n=8-15. (a) recombinant WA-1 (rWA-1), (b) ΔORF6, (c) ΔORF8.

Next, we analyzed cytokine levels in URT and lung samples from index mice by multiplex ELISA (**Fig. 4g**). We found that cytokine levels present in the URT of mice infected with ΔORF8 had a similar magnitude to those infected with rWA-1 and ΔORF6, despite 100-fold lower WA-1 ΔORF8 titers at the same time point (2 dpi). This suggests increased inflammatory signature of ΔORF8 relative to amount of virus present in the URT. In lungs, which display similar viral titers across the three viruses (**Fig. 4g**), we observed a similar pattern of cytokines between ΔORF8- and rWA-1-infected mice (**Fig. 4g**). How and whether inflammation by ΔORF8 attenuates viral replication specifically in the URT, but not in the lungs, remains the topic of further investigation. Of note, cytokine

levels were elevated in ΔORF6-infected lungs compared to both rWA-1- and ΔORF8-infected lungs, particularly IL-6, suggesting that the recombinant virus lacking ORF6 is unable to suppress production of certain cytokines in the lungs of neonatal mice.

Taken together our results show how removal of one SARS-CoV-2 accessory protein, ORF8, reduces URT replication, resulting in reduced shedding and transmission in neonatal mice. Our neonatal mouse model allows for a unique view on these molecular processes in spatial granularity, and the availability of mouse-specific reagents will enable future mechanistic studies on the role of ORF8 in URT replication and transmission.

Discussion

Mouse models of SARS-CoV-2 infection have been utilized extensively to study the pathogenesis of emerging SARS-CoV-2 variants[46-52]. However, adult mice do not robustly transmit SARS-CoV-2 (**Supplemental Fig. 1a-f** and [3]). In our study, we developed and validated a neonatal mouse model to characterize the transmission of SARS-CoV-2 human isolates based on our previous experience with influenza A virus (**Fig. 1** and [18]). Using a unique SARS-CoV-2 panel spanning early to current pandemic human isolates, we demonstrate how variant-inherent mutations affect tropism and shedding (**Fig. 2**), transmission (**Fig. 3**), and upper respiratory tract cytokine repertoires (**Supplemental Fig. 4**). Finally, our study reveals a previously unappreciated role for the accessory protein ORF8 in viral upper respiratory tract replication, inflammation, and transmission in neonatal mice (**Fig. 4**), displaying the power of our model to study the viral and host molecular determinants of SARS-CoV-2 transmission in mice.

Our model has several advantages over existing animal models of SARS-CoV-2 transmission: First, amenability to a wide range of available knockout animals allows for future systematic studies determining host factors that are critical for transmission. Second, our model allows for powered studies, as high numbers of contact neonatal mice are more easily achieved than in other animal models. Third, there are fewer husbandry challenges to work with mice as compared to hamsters or ferrets. Further, the availability of mouse-specific reagents and tools increases the potential to study virus-induced immune pathways in the host, as well as respiratory mechanics that could impact transmission, such as air flow and lung capacity. Finally, we can track the index's progression and contact infection longitudinally, due to non-invasive sampling. This provides more granularity and insight into the kinetics of viral shedding and URT viral load at the level of individuals, which illuminates our understanding of transmission efficiency.

Although these features establish our model as a unique and workable tool for studying SARS-CoV-2 transmission, other animal models, such as hamsters and ferrets, have certain advantages over the limitations of our system. One limitation of our model is that the modes of transmission cannot be tested experimentally, because suckling mice cannot be separated from each other or their mother. It is likely that transmission in the model, like in humans[53,54], occurs via a combination of modes. Long-range aerosol transmission, as can occur in humans[55], cannot be measured in our current experimental setup. Nevertheless, the model features behavioral situations favorable for both influenza virus and SARS-CoV-2 transmission, as shown both in humans and in more classical animal model systems: prolonged time of exposure[56], proximity of individuals in enclosed spaces[57] and cohabitation with household members[54,58-60]. In addition, our non-invasive

sample collection method from individual pups allows us to longitudinally measure temporal dynamics and amplitude of viral shedding, both factors that are critical in respiratory virus transmission[18,33,34,61-63]. Another limitation of our model is that the expression of the hACE2 transgene is driven by a non-native K18 promoter, allowing the infection of multiple organs, and resulting in tissue expression levels that are distinct from endogenously expressed murine Ace2[49,50]. Although the expression is non-physiological, we deliberately chose K18-hACE2 mice for this first study of SARS-CoV-2 transmission in mice since our goal was to investigate and compare transmission of early and current pandemic isolates, some of which are unable to engage murine Ace2. We recognize that extrapolating tropism changes in our model to tropism in humans warrants caution, especially if these changes are solely brought upon by changes in variant spike-ACE2 binding, i.e., through mutations in spike's receptor binding site. However, we argue that tropism changes brought upon by differences in spike processing and/or by differences in host-virus interplay can be readily interpreted using our model, since protease expression and inflammation or antagonism are unadulterated by the hACE2 transgene. Taken together, our study demonstrates how the selection among available animal models should be based on research scope and context, as each of them can provide valuable and non-redundant information regarding SARS-CoV-2 biology.

In our model, except for Omicron BA.1, we observed at or above 33% SARS-CoV-2 variant transmission, and our method was granular enough to detect subtle differences between variants. For example, we identified an early but narrow peak of URT replication for Alpha, leaving only a short window for transmission. Despite this, contact animals acquire Alpha at a similar rate to ancestral WA-1, and even display significantly higher

contact titers at 3 dpi. In fact, Alpha was the only virus with similar or better transmission efficiency to WA-1, while all other variants displayed a significant delay in transmission compared to WA-1. Variants post-Alpha arose after widespread population immunity brought by either prior infection or immunization, and viral evasion from neutralization due to mutations in the variants' spike gene is well-documented[64-70]. Thus, we speculate that transmission differences between WA-1 and variants Beta to Delta may have been less dramatic under adaptive immune pressure or even reveal a transmission advantage for these variants compared to the ancestral virus, to which most immunization regimens are currently matched. Future studies with this model will introduce adaptive immune pressures by vaccination of dams prior to pregnancy. Offspring will acquire immunoglobulins via transplacental passage or milk, which has been shown to reduce transmission in our influenza A virus model[18].

SARS-CoV-2's accessory protein ORF8 is arguably the most enigmatic, as it only shares a 20% protein identity with SARS-CoV. For SARS-CoV-2, ORF8 is a secreted glycoprotein[40,71,72], and diverse immunomodulatory functions have been proposed, such as IL-17A mimicry[73,74], interference with the interferon type I pathway[43], histone mimicry[75], and downregulation of MHC class I[76,77], although the full spectrum of ORF8's functions and mechanisms of action remain to be elucidated[78]. In our model, deletion of ORF8 resulted in reduced replication specifically in the URT. The magnitude of inflammatory cytokines (**Fig. 4**) we observe for ΔORF8 in the URT was similar to those of parental WA-1 or ΔORF6 virus, despite 100-fold less virus in that compartment. This increased inflammation was similar to previous observations in adult K18-hACE mice[41,45]. It is feasible that, without ORF8, SARS-CoV-2 fails to suppress critical antiviral responses in

537 the URT. We argue that the reduced URT replication and consequent decrease in
538 shedding, is the cause of ΔORF8's delayed and reduced transmission in mice. We further
539 argue that this is not due to an overall attenuation of SARS-CoV-2 lacking ORF8, as these
540 viruses replicate efficiently in tissue culture and in the lungs of both neonatal and adult
541 K18-hACE2 mice (**Fig. 4** and[45]). To our knowledge, this is the first report of a
542 compartment-specific role of a SARS-CoV-2 accessory protein in mice. Although
543 underlying mechanisms for the URT-specific role of ORF8 remain unknown, it is possible
544 that antiviral inflammatory processes brought upon by SARS-CoV-2 infection are different
545 in the URT from those in the lower respiratory tract. For instance, the cellular milieu and
546 temperature differences between the URT and LRT may play a role in the behavior of the
547 virus and response to infection in these compartments. Furthermore, the poor
548 conservation of ORF8 among related coronaviruses[78], the appearance of a 382-
549 nucleotide deletion in the ORF8 of SARS-CoV-2 isolates in patients during February 2020
550 and the circulation of a SARS-CoV-2 isolate containing a truncated version of ORF8 from
551 March through October 2020[79] suggest that ORF8 is a hotspot for SARS-CoV-2
552 adaptation and evolution[78]. For example, the Alpha variant, which we also characterized
553 in our study, carries a stop codon at amino acid 27 of ORF8, resulting in the expression
554 of a truncated ORF8 protein[4]. Interestingly, in our model, ΔORF8 and Alpha did not
555 phenocopy in terms of URT replication, cytokine responses, or transmission. It is possible
556 that alpha's truncated ORF8 retains functions that are critical for URT replication. Another
557 possibility is that alpha's ORF8 is defunct, but that other viral proteins, some of which are
558 different from the WA-1 background, provide redundant immune suppression

mechanisms that compensate for the lack of ORF8 action in Alpha. Future studies with additional recombinant SARS-CoV-2 will enable detangling the different hypotheses.

What are the determinants of SARS-CoV-2 transmission in our model? Our data suggest that the level of infectious index shedding titer matters with respect to transmission efficiency. We find that lower levels of index shedding are correlated with reduced transmission efficiency, as shown by both tested Omicron variants and by ΔORF8. Further, we observe that early timing of peak in index shedding (1 dpi vs 2 or 3 dpi) favors transmission efficiency, as shown by the slight transmission advantage of Alpha over WA-1 and the clear transmission advantage of Omicron BQ.1.1 over BA.1. Finally, we find that URT viral titers correlate with shedding titers across all viruses tested in this study, suggesting overall that efficient, early-onset URT replication determines SARS-CoV-2 transmission efficiency in our model. In contrast, in our model, we found that there was no association between the shedding of SARS-CoV-2 and the viral titers in the LRT, which suggests that the virus present in the lungs may be primarily responsible for causing disease, rather than facilitating its transmission.

In summary, we established a SARS-CoV-2 transmission model using neonatal K18-hACE2 transgenic mice that characterizes the net effect of variant-inherent mutations on viral tropism and transmission and uncovers for the first time the contribution of accessory proteins to transmission. Using this tractable animal model to define the molecular mechanisms underlying SARS-CoV-2 transmission could guide the development of superior antiviral therapies and contribute to a greater understanding of not only SARS-CoV-2, but respiratory viruses in general.

Methods

Cell lines

Vero E6 cells were cultured in Dulbecco modified Eagle medium (DMEM) (Gibco) supplemented with 10% fetal bovine serum (FBS) (Atlanta Biologicals), 1% Pen/Strep (Gibco) and 1% Amphotericin B (Gibco) at 37°C with 5% CO2. Vero E6-TMPRSS2-T2A-ACE2 cells were cultured in DMEM (Corning) containing 4 mM L-glutamine, 4500 mg per L glucose, 1 mM sodium pyruvate and 1500 mg per L sodium bicarbonate, supplemented with 10% fetal bovine serum and 10 µg per mL puromycin (Sigma) at 37°C with 5% CO_2. All cell lines were confirmed to be mycoplasma free.

Mice

C57BL/6J and K18-hACE2 C57BL/6J (strain 2B6.Cg-Tg(K18-ACE2)2Prlmn/J) mice (Jackson Laboratories, ME) were maintained and bred in a conventional animal facility. To produce neonatal heterozygous K18-hACE2 C57BL/6J mice for the transmission experiments, C57BL/6J females were bred with homozygous K18-hACE2 C57BL/6J males. Pups were housed with their mother during all experiments. Animal experiments were performed in the Animal Biosafety Level 3 (ABSL3) facility of NYU Grossman School of Medicine (New York, NY), in accordance with its Biosafety Manual and Standard Operating Procedures and following Institutional Animal Care and Use Committee (IACUC) guidelines.

Biosafety and work with biohazardous material

All work with infectious SARS-CoV-2 isolates and recombinant viruses, including work with infected animals, was performed in the Animal Biosafety Level 3 (ABSL3) facilities of the University of Maryland (Baltimore, MD) and NYU Grossman School of Medicine (New York, NY). Both facilities are registered with their respective local Departments of Health and passed inspections by the Centers for Disease Control & Prevention (CDC (Centers for Disease Control)) within the year of submission of this manuscript. ABSL3 facilities are operated in accordance with their Biosafety Manuals and Standard Operating Procedures, including for the containment of biohazardous aerosols using certified biosafety cabinets and the facilities' sealed ventilation systems that provide a sustained directional airflow, from clean towards potentially contaminated areas, and HEPA-filtered exhaust. Biohazardous waste generated in the facilities is fully decontaminated using approved disinfectants followed by autoclaving and incineration as Regulated Medical waste. Access to ABSL3 facilities is restricted to certified and authorized personnel, enrolled into occupational health surveillance programs, and wearing adequate Personal Protective Equipment (PPE), including OSHA-approved respirators, eye protection, spill-resistant coveralls, and double-gloves. When analyzed outside of ABSL3 facilities, infectious samples were thoroughly treated using vetted inactivation methods.

All work with infectious SARS-CoV-2 isolates and recombinant viruses was performed with prior approval of the Institutional Biosafety Committees (IBCs) of the University of Maryland School of Medicine and NYU Grossman School of Medicine. Import permits for SARS-CoV-2 variant isolates were approved by the CDC. Generation of recombinant SARS-CoV-2 viruses was approved for M.F. by the IBC (Institutional Biosafety Committee) of the University of Maryland School of Medicine.

Generation of Virus Stocks

The following reagents were obtained through BEI Resources, NIAID, NIH (National Institutes of Health): SARS-Related Coronavirus 2, Isolate USA-WA1/2020, NR-52281, deposited by the Centers for Disease Control and Prevention; SARS-Related Coronavirus 2, Isolate hCoV-19/England/204820464/2020, B.1.1.7, NR-54000, contributed by Bassam Hallis; SARS-Related Coronavirus 2, Isolate hCoV-19/South Africa/KRISP-K005325/2020, B.1.351, NR-54009, contributed by Alex Sigal and Tulio de Oliveira; SARS-Related Coronavirus 2, Isolate hCoV-19/Japan/TY7-503/2021 (Brazil P.1), NR-54982, contributed by National Institute of Infectious Diseases. SARS-CoV-2 Delta variant (hCoV19/USA/PHC658/2021) and SARS-CoV-2 Omicron BA.1 (hCoV-19/USA/GA-EHC-2811C/2021) were kindly provided by the Suthar Lab at Emory University. SARS-CoV-2 hCoV-19/USA/CA-Stanford-106_S04/2022 (Omicron BQ1.1, EPI_ISL_15196219) was obtained from Dr. Mehul Suthar (Emory University, Atlanta, Georgia, USA) and Dr. Benjamin Pinsky (Stanford University, Stanford, California, USA). The USA-WA1/2020 stock was produced as previously described[80]. The other SARS-CoV-2 viruses were passaged once in Vero E6 cells supplemented with 1 µg/ml of l-1-tosylamido-2-phenylethyl chloromethyl ketone (TPCK)-trypsin, to avoid virus adaptation to Vero E6 cells due to the lack of TMPRSS2 expression. Cells were infected at an MOI of 0.01 and harvested at 50% cytopathic effect (CPE). After harvest, the virus was purified using a 25% sucrose cushion at 25,000 RPM for 3-4 hours and resuspended using PBS (Phosphate Buffered Saline) prior to infection. For the B.1.1.7, B.1.1.351 and P.1, stocks, aliquots were initially plaque-purified and sequenced to verify the variant signature before

expanding in the presence of TPCK-trypsin to generate a passage 1 working stock. We perform a cellular debris exclusion step by benchtop centrifugation prior to proceeding with the virus pelleting step through a sucrose cushion. We then resuspend the pellet in a low volume, resulting in highly concentrated, purified SARS-CoV-2 stocks. WA-1 ΔORF6, WA-1ΔORF8 and its WA-1 control were generated in the Frieman Lab at University of Maryland School of Medicine[62]; aliquots were used as provided for the experiments. For heat-inactivated (HI) SARS-CoV-2 WA-1, viral stocks were incubated at 56ºC for 5 hours. Samples were titered for confirmation of complete inactivation of infectious particles.

Immunohistochemistry on mouse heads

Pups infected as described above were euthanized according to humane, IACUC-approved procedure at 2 dpi. The skin of heads was gently removed to preserve nasal structures. Heads were then removed and submerged in PBS at 4°C for a brief wash, followed by fixing in 4% paraformaldehyde for 72 h at 4°C without shaking. Heads were then washed in PBS at 4°C with gentle swirling for 20 min, followed by decalcification into 0.12M EDTA solution at 4°C with gentle shaking for 7 days. Intact heads were then processed through graded ethanols to xylene and infiltrated with paraffin in a Leica Peloris automated tissue processor. Paraffin-embedded sections were immunostained on a Leica BondRX, according to manufacturer's instructions. In brief, deparaffinized sections underwent a 20-minute heat retrieval in Leica ER2 buffer (pH9, AR9640) followed by Rodent Block (Biocare, RBM961 L) prior to a one-hour incubation with SARS-CoV-2 N protein antibody (clone 1C7C7) at a 1:300 dilution and a AF594-conjugated Goat-anti-

mouse secondary (ThermoFisher, A11005). Slides were counterstained with DAPI and scanned on an Akoya Polaris Vectra imaging system. Images were viewed and prepared with Akoya Phenochart and OMERO software prior to exporting as TIF files.

SARS-CoV-2 infection of adult mice

Adult C57BL/6J K18-hACE2 +/- hemizygous mice (13 weeks of age) were infected with a lethal dose (10,000 PFU) of ancestral SARS-CoV-2 USA_WA-1/2020 via a 10 µL intranasal infection under Ketamine/Xylazine anesthesia. Male and female mice were housed separately in groups of four at a 1:3 infected index to uninfected contact ratio. Shedding of virus was collected by dipping the nares of each mouse three times into viral medium (PBS plus 0.3% bovine serum albumin [BSA]) daily for 10 days. Intra-cage transmission was determined by infectious particle presence in contact mice. % Acquisition was scored and presented as described below. Moribund were euthanized by CO_2 asphyxiation followed by cervical dislocation when humane endpoint criteria were met . At 10 dpi, surviving animals were euthanized by CO_2 asphyxiation followed by cardiac puncture. Retro tracheal lavages of the upper respiratory tracts of surviving animals were conducted by pushing 500 µL of sterile PBS through the trachea and out the nares. Lungs were collected and homogenized with stainless steel beads as described below.

To assess seroconversion due to transmission, adult mice (male and female) were infected as described above and housed separately in groups of 1:3 and 1:2 infected index: uninfected contacts. 13-week-old male mice were inoculated with 10 µL sterile PBS and 12-week-old female mice were inoculated with a 10 µL sublethal dose of SARS-CoV-

2 USA_WA-1/2020 (1000 PFU). Mice were monitored daily for weight and survival. At 3 weeks post infection, animals were euthanized by CO_2 asphyxiation followed by cardiac puncture. Retro tracheal lavage of the URT and lung homogenates were collected as described above. Blood was collected via cardiac puncture using a 1mL 28G1/2 insulin syringe and added to a serum collection tube (BD Microtainer 365967). Tubes were incubated for 45 minutes at room temperature to facilitate blood coagulation and then spun at 4 °C for 10 minutes (1500 x g). Serum was separated, frozen at -80 °C, and analyzed for presence of IgG antibodies against Spike Trimer (Acro Biosystems RAS-T023).

SARS-CoV-2 infection of neonatal mice, determination of shedding and transmission.

Index pups in a litter (4 to 7 days of age) were infected with a 3 µL sterile PBS inoculum without general anesthesia (to avoid direct lung inoculation) by intranasal instillation of 1500 PFU of SARS-CoV-2 WA-1, SARS-CoV-2 variant or recombinant SARS-CoV-2 and returned to the litter for the duration of the experiment. Shedding of virus was collected by dipping the nares of each mouse three times into viral medium (PBS plus 0.3% bovine serum albumin [BSA]) daily, and samples were evaluated via quantitative reverse transcription-PCR (RT-qPCR) or plaque assay. Intra-litter transmission was assessed by collecting shedding samples daily in the littermates (contact). % Acquisition was visualized in inverted Kaplan-Meier plots. Acquisition events were scored as at least two days of infectious viral titer in shedding samples. The onset of acquisition was scored as the first day of infectious virus detection. The pups and mother were euthanized by CO_2

asphyxiation followed by cardiac puncture. The upper respiratory tract (URT) was subjected to a retro tracheal lavage (flushing of 300 µL PBS from the trachea and collecting through the nares), and samples were used to quantify viruses (via plaque assay or qRT-PCR). Ratios of index to contact pups ranged from 1:6-9 for variant comparison to 1:3-1:4 for model optimization with WA-1.

SARS-CoV-2 quantification RT-qPCR

RNA extractions were performed using the Qiagen QIAamp Viral RNA kit. The number of viral N copy number per µL was quantified by RT-qPCR using the Taqman® RNA-to-CT One-Step RT-PCR kit (Applied Biosystems™) with SARS-CoV-2 primers and probe targeting an amplicon in the N protein of SARS-CoV-2 WA-1 (Forward: 5'ATGCTGCAATCGTGCTACAA3'; reverse: 5' GACTGCCGCCTCTGCTC3') and the probe 5'/56-FAM/TCAAGGAAC/ZEN/AACATTGCCAA/3IABkFQ/3'. A standard curve was generated for each dataset using in vitro transcribed SARS-CoV-2 N RNA sequence (MN985325.1).

SARS-CoV-2 infectious titer quantification

Infectious viral titers were determined by plaque assay. In brief, 10-fold dilutions of each virus in DMEM + 1% antibiotic/antimycotic (Gibco) were added to a monolayer Vero E6-TMPRSS2-T2A-ACE2 cells for 1 h at 37ºC. Following incubation, cells were overlaid with 0.8% agarose in DMEM containing 2% FBS and incubated at 37ºC for 36 hrs. Cells were fixed with 10% formalin, the agarose plug removed, and plaques visualized by crystal

violet staining. Stocks and samples obtained from mouse experiments (shedding, lavage, and lung homogenates) were tittered in Vero E6-TMPRSS2-T2A-ACE2.

Lung SARS-CoV-2 titer quantification

Lungs were collected in 500 µL of DPBS containing one stainless steel bead (QIAGEN), homogenized with the Tissue-Lyser II (QIAGEN), and debris were pulled down at 8000 rpm for 8 min. Viral titers were determined by plaque assay using Vero E6-TMPRSS2-T2A-ACE2 cells.

Cytokine and chemokine protein measurements

Cytokine and chemokine levels were measured in mouse serum using the Bio-Plex Pro Mouse Cytokine 23-plex Assay (Bio-Rad). Cytokines and chemokines were recorded on a MAGPIX machine (Luminex) and quantitated via comparison to a standard curve. xPONENT version 4.3.229.0 software was used for the data collection and analysis. We used the experimentally obtained limits of detection for each protein and set values below that limit of detection to one log below the limit. All samples were normalized to those from PBS-treated animals. Clustered heatmaps were generated using the ComplexHeatmap package in program R v.4.1.2.

Quantification and statistical analysis

All statistical analyses were performed using GraphPad Prism 9.5. Each experiment was completed at least two independent times with internal biological duplicates unless otherwise noted in the figure legends. The exact number of biological replicates (n) can

be found in the figure legends. Data are represented as the geometric mean ± geometric standard deviation (SD). Kruskal-Wallis, one-way ANOVA test with Bonferroni post hoc test and log-rank Mantel-Cox tests were performed and specifically indicated in the figure legends. Only p-values < 0.05 were displayed in the figures and p-values > 0.05 were considered non-significant (ns).

Data availability

All data are included in this article and Supplementary Information. Any additional information required to reanalyze the data reported in this paper is available from the corresponding authors upon request.

References

1 Richard, M. *et al.* SARS-CoV-2 is transmitted via contact and via the air between ferrets. *Nat Commun* **11**, 3496 (2020). https://doi.org:10.1038/s41467-020-17367-2

2 Sia, S. F. *et al.* Pathogenesis and transmission of SARS-CoV-2 in golden hamsters. *Nature* **583**, 834-838 (2020). https://doi.org:10.1038/s41586-020-2342-5

3 Pan, T. *et al.* Infection of wild-type mice by SARS-CoV-2 B.1.351 variant indicates a possible novel cross-species transmission route. *Signal Transduct Target Ther* **6**, 420 (2021). https://doi.org:10.1038/s41392-021-00848-1

4 *https://covariants.org*.

5 Kyriakidis, N. C., Lopez-Cortes, A., Gonzalez, E. V., Grimaldos, A. B. & Prado, E. O. SARS-CoV-2 vaccines strategies: a comprehensive review of phase 3 candidates. *NPJ Vaccines* **6**, 28 (2021). https://doi.org:10.1038/s41541-021-00292-w

6 Zhou, P. *et al.* A pneumonia outbreak associated with a new coronavirus of probable bat origin. *Nature* **579**, 270-273 (2020). https://doi.org:10.1038/s41586-020-2012-7

7 Hu, B., Guo, H., Zhou, P. & Shi, Z. L. Characteristics of SARS-CoV-2 and COVID-19. *Nat Rev Microbiol* **19**, 141-154 (2021). https://doi.org:10.1038/s41579-020-00459-7

8 Minkoff, J. M. & tenOever, B. Innate immune evasion strategies of SARS-CoV-2. *Nat Rev Microbiol* **21**, 178-194 (2023). https://doi.org:10.1038/s41579-022-00839-1

9 Xia, H. *et al.* Evasion of Type I Interferon by SARS-CoV-2. *Cell Rep* **33**, 108234 (2020). https://doi.org:10.1016/j.celrep.2020.108234

10 Kopecky-Bromberg, S. A., Martinez-Sobrido, L., Frieman, M., Baric, R. A. & Palese, P. Severe acute respiratory syndrome coronavirus open reading frame (ORF) 3b, ORF 6, and nucleocapsid proteins function as interferon antagonists. *J Virol* **81**, 548-557 (2007). https://doi.org:10.1128/JVI.01782-06

11 Konno, Y. *et al.* SARS-CoV-2 ORF3b Is a Potent Interferon Antagonist Whose Activity Is Increased by a Naturally Occurring Elongation Variant. *Cell Rep* **32**, 108185 (2020). https://doi.org:10.1016/j.celrep.2020.108185

12 Schroeder, S. *et al.* Interferon antagonism by SARS-CoV-2: a functional study using reverse genetics. *Lancet Microbe* **2**, e210-e218 (2021). https://doi.org:10.1016/S2666-5247(21)00027-6

13 Shemesh, M. *et al.* SARS-CoV-2 suppresses IFNbeta production mediated by NSP1, 5, 6, 15, ORF6 and ORF7b but does not suppress the effects of added interferon. *PLoS Pathog* **17**, e1009800 (2021). https://doi.org:10.1371/journal.ppat.1009800

14 Callaway, E. What Omicron's BA.4 and BA.5 variants mean for the pandemic. *Nature* **606**, 848-849 (2022). https://doi.org:10.1038/d41586-022-01730-y

15 Lamers, M. M. & Haagmans, B. L. SARS-CoV-2 pathogenesis. *Nat Rev Microbiol* **20**, 270-284 (2022). https://doi.org:10.1038/s41579-022-00713-0

16 Liu, Z. *et al.* Landscape analysis of escape variants identifies SARS-CoV-2 spike mutations that attenuate monoclonal and serum antibody neutralization. *bioRxiv* (2021). https://doi.org:10.1101/2020.11.06.372037

817 17 Imai, M. *et al.* Syrian hamsters as a small animal model for SARS-CoV-2 infection and
818 countermeasure development. *Proc Natl Acad Sci U S A* **117**, 16587-16595 (2020).
819 https://doi.org:10.1073/pnas.2009799117
820 18 Ortigoza, M. B., Blaser, S. B., Zafar, M. A., Hammond, A. J. & Weiser, J. N. An Infant
821 Mouse Model of Influenza Virus Transmission Demonstrates the Role of Virus-Specific
822 Shedding, Humoral Immunity, and Sialidase Expression by Colonizing Streptococcus
823 pneumoniae. *mBio* **9** (2018). https://doi.org:10.1128/mBio.02359-18
824 19 Rodewald, A. K., Onderdonk, A. B., Warren, H. B. & Kasper, D. L. Neonatal mouse model
825 of group B streptococcal infection. *J Infect Dis* **166**, 635-639 (1992).
826 https://doi.org:10.1093/infdis/166.3.635
827 20 Abruzzo, A. R., Aggarwal, S. D., Sharp, M. E., Bee, G. C. W. & Weiser, J. N. Serotype-
828 Dependent Effects on the Dynamics of Pneumococcal Colonization and Implications for
829 Transmission. *mBio* **13**, e0015822 (2022). https://doi.org:10.1128/mbio.00158-22
830 21 Zafar, M. A. *et al.* Identification of Pneumococcal Factors Affecting Pneumococcal
831 Shedding Shows that the dlt Locus Promotes Inflammation and Transmission. *mBio* **10**
832 (2019). https://doi.org:10.1128/mBio.01032-19
833 22 Zafar, M. A., Kono, M., Wang, Y., Zangari, T. & Weiser, J. N. Infant Mouse Model for the
834 Study of Shedding and Transmission during Streptococcus pneumoniae Monoinfection.
835 *Infect Immun* **84**, 2714-2722 (2016). https://doi.org:10.1128/IAI.00416-16
836 23 Zangari, T., Ortigoza, M. B., Lokken-Toyli, K. L. & Weiser, J. N. Type I Interferon Signaling
837 Is a Common Factor Driving Streptococcus pneumoniae and Influenza A Virus Shedding
838 and Transmission. *mBio* **12** (2021). https://doi.org:10.1128/mBio.03589-20
839 24 Compton, S. R., Paturzo, F. X. & Macy, J. D. Transmission of mouse parvovirus to
840 neonatal mice. *J Am Assoc Lab Anim Sci* **51**, 797-802 (2012).
841 25 Han, P. *et al.* Receptor binding and complex structures of human ACE2 to spike RBD
842 from omicron and delta SARS-CoV-2. *Cell* **185**, 630-640 e610 (2022).
843 https://doi.org:10.1016/j.cell.2022.01.001
844 26 Huang, H., Zhu, Y., Niu, Z., Zhou, L. & Sun, Q. SARS-CoV-2 N501Y variants of concern and
845 their potential transmission by mouse. *Cell Death Differ* **28**, 2840-2842 (2021).
846 https://doi.org:10.1038/s41418-021-00846-4
847 27 McCray, P. B., Jr. *et al.* Lethal infection of K18-hACE2 mice infected with severe acute
848 respiratory syndrome coronavirus. *J Virol* **81**, 813-821 (2007).
849 https://doi.org:10.1128/JVI.02012-06
850 28 Lowen, A. C., Mubareka, S., Tumpey, T. M., Garcia-Sastre, A. & Palese, P. The guinea pig
851 as a transmission model for human influenza viruses. *Proc Natl Acad Sci U S A* **103**, 9988-
852 9992 (2006). https://doi.org:10.1073/pnas.0604157103
853 29 Edenborough, K. M., Gilbertson, B. P. & Brown, L. E. A mouse model for the study of
854 contact-dependent transmission of influenza A virus and the factors that govern
855 transmissibility. *J Virol* **86**, 12544-12551 (2012). https://doi.org:10.1128/JVI.00859-12
856 30 Rosenke, K. *et al.* UK B.1.1.7 (Alpha) variant exhibits increased respiratory replication
857 and shedding in nonhuman primates. *Emerg Microbes Infect* **10**, 2173-2182 (2021).
858 https://doi.org:10.1080/22221751.2021.1997074

859 31 von Wintersdorff, C. J. H. *et al.* Infections with the SARS-CoV-2 Delta variant exhibit
860 fourfold increased viral loads in the upper airways compared to Alpha or non-variants of
861 concern. *Sci Rep* **12**, 13922 (2022). https://doi.org:10.1038/s41598-022-18279-5
862 32 Yan, J. *et al.* Infectious virus in exhaled breath of symptomatic seasonal influenza cases
863 from a college community. *Proc Natl Acad Sci U S A* **115**, 1081-1086 (2018).
864 https://doi.org:10.1073/pnas.1716561115
865 33 Danzy, S., Lowen, A. C. & Steel, J. A quantitative approach to assess influenza A virus
866 fitness and transmission in guinea pigs. *J Virol* **95** (2021).
867 https://doi.org:10.1128/JVI.02320-20
868 34 Mubareka, S. *et al.* Transmission of influenza virus via aerosols and fomites in the guinea
869 pig model. *J Infect Dis* **199**, 858-865 (2009). https://doi.org:10.1086/597073
870 35 Port, J. R. *et al.* Host and viral determinants of airborne transmission of SARS-CoV-2 in
871 the Syrian hamster. *bioRxiv* (2023). https://doi.org:10.1101/2022.08.15.504010
872 36 Yuan, S. *et al.* Pathogenicity, transmissibility, and fitness of SARS-CoV-2 Omicron in
873 Syrian hamsters. *Science* **377**, 428-433 (2022). https://doi.org:10.1126/science.abn8939
874 37 Halfmann, P. J. *et al.* SARS-CoV-2 Omicron virus causes attenuated disease in mice and
875 hamsters. *Nature* **603**, 687-692 (2022). https://doi.org:10.1038/s41586-022-04441-6
876 38 Boon, A. C. M. *et al.* Reduced airborne transmission of SARS-CoV-2 BA.1 Omicron virus in
877 Syrian hamsters. *PLoS Pathog* **18**, e1010970 (2022).
878 https://doi.org:10.1371/journal.ppat.1010970
879 39 Leung, N. H. L. Transmissibility and transmission of respiratory viruses. *Nat Rev*
880 *Microbiol* **19**, 528-545 (2021). https://doi.org:10.1038/s41579-021-00535-6
881 40 Silvas, J. A. *et al.* Contribution of SARS-CoV-2 Accessory Proteins to Viral Pathogenicity in
882 K18 Human ACE2 Transgenic Mice. *J Virol* **95**, e0040221 (2021).
883 https://doi.org:10.1128/JVI.00402-21
884 41 Liu, Y. *et al.* A live-attenuated SARS-CoV-2 vaccine candidate with accessory protein
885 deletions. *Nat Commun* **13**, 4337 (2022). https://doi.org:10.1038/s41467-022-31930-z
886 42 Kehrer, T. *et al.* Impact of SARS-CoV-2 ORF6 and its variant polymorphisms on host
887 responses and viral pathogenesis. *bioRxiv* (2022).
888 https://doi.org:10.1101/2022.10.18.512708
889 43 Li, J. Y. *et al.* The ORF6, ORF8 and nucleocapsid proteins of SARS-CoV-2 inhibit type I
890 interferon signaling pathway. *Virus research* **286**, 198074 (2020).
891 https://doi.org:10.1016/j.virusres.2020.198074
892 44 Miorin, L. *et al.* SARS-CoV-2 Orf6 hijacks Nup98 to block STAT nuclear import and
893 antagonize interferon signaling. *Proc Natl Acad Sci U S A* **117**, 28344-28354 (2020).
894 https://doi.org:10.1073/pnas.2016650117
895 45 McGrath, M. E. *et al.* SARS-CoV-2 variant spike and accessory gene mutations alter
896 pathogenesis. *Proc Natl Acad Sci U S A* **119**, e2204717119 (2022).
897 https://doi.org:10.1073/pnas.2204717119
898 46 Bayarri-Olmos, R. *et al.* The alpha/B.1.1.7 SARS-CoV-2 variant exhibits significantly
899 higher affinity for ACE-2 and requires lower inoculation doses to cause disease in K18-
900 hACE2 mice. *Elife* **10** (2021). https://doi.org:10.7554/eLife.70002
901 47 Shuai, H. *et al.* Attenuated replication and pathogenicity of SARS-CoV-2 B.1.1.529
902 Omicron. *Nature* **603**, 693-699 (2022). https://doi.org:10.1038/s41586-022-04442-5

48 Horspool, A. M. *et al.* SARS-CoV-2 B.1.1.7 and B.1.351 variants of concern induce lethal disease in K18-hACE2 transgenic mice despite convalescent plasma therapy. *bioRxiv* (2021). https://doi.org:10.1101/2021.05.05.442784

49 Winkler, E. S. *et al.* SARS-CoV-2 Causes Lung Infection without Severe Disease in Human ACE2 Knock-In Mice. *J Virol* **96**, e0151121 (2022). https://doi.org:10.1128/JVI.01511-21

50 Winkler, E. S. *et al.* SARS-CoV-2 infection of human ACE2-transgenic mice causes severe lung inflammation and impaired function. *Nat Immunol* **21**, 1327-1335 (2020). https://doi.org:10.1038/s41590-020-0778-2

51 Zhang, Y. *et al.* SARS-CoV-2 rapidly adapts in aged BALB/c mice and induces typical pneumonia. *J Virol* **95** (2021). https://doi.org:10.1128/JVI.02477-20

52 Yasui, F. *et al.* Infection with the SARS-CoV-2 B.1.351 variant is lethal in aged BALB/c mice. *Sci Rep* **12**, 4150 (2022). https://doi.org:10.1038/s41598-022-08104-4

53 Ribaric, N. L., Vincent, C., Jonitz, G., Hellinger, A. & Ribaric, G. Hidden hazards of SARS-CoV-2 transmission in hospitals: A systematic review. *Indoor Air* **32**, e12968 (2022). https://doi.org:10.1111/ina.12968

54 Cowling, B. J. *et al.* Aerosol transmission is an important mode of influenza A virus spread. *Nat Commun* **4**, 1935 (2013). https://doi.org:10.1038/ncomms2922

55 Duval, D. *et al.* Long distance airborne transmission of SARS-CoV-2: rapid systematic review. *BMJ* **377**, e068743 (2022). https://doi.org:10.1136/bmj-2021-068743

56 Ganti, K. *et al.* Timing of exposure is critical in a highly sensitive model of SARS-CoV-2 transmission. *PLoS Pathog* **18**, e1010181 (2022). https://doi.org:10.1371/journal.ppat.1010181

57 Moon, J. & Ryu, B. H. Transmission risks of respiratory infectious diseases in various confined spaces: A meta-analysis for future pandemics. *Environ Res* **202**, 111679 (2021). https://doi.org:10.1016/j.envres.2021.111679

58 Poon, L. L. *et al.* Viral genetic sequence variations in pandemic H1N1/2009 and seasonal H3N2 influenza viruses within an individual, a household and a community. *J Clin Virol* **52**, 146-150 (2011). https://doi.org:10.1016/j.jcv.2011.06.022

59 Madewell, Z. J., Yang, Y., Longini, I. M., Jr., Halloran, M. E. & Dean, N. E. Household Transmission of SARS-CoV-2: A Systematic Review and Meta-analysis. *JAMA Netw Open* **3**, e2031756 (2020). https://doi.org:10.1001/jamanetworkopen.2020.31756

60 Baker, J. M. *et al.* SARS-CoV-2 B.1.1.529 (Omicron) Variant Transmission Within Households - Four U.S. Jurisdictions, November 2021-February 2022. *MMWR Morb Mortal Wkly Rep* **71**, 341-346 (2022). https://doi.org:10.15585/mmwr.mm7109e1

61 Puhach, O., Meyer, B. & Eckerle, I. SARS-CoV-2 viral load and shedding kinetics. *Nat Rev Microbiol* **21**, 147-161 (2023). https://doi.org:10.1038/s41579-022-00822-w

62 Cevik, M. *et al.* SARS-CoV-2, SARS-CoV, and MERS-CoV viral load dynamics, duration of viral shedding, and infectiousness: a systematic review and meta-analysis. *Lancet Microbe* **2**, e13-e22 (2021). https://doi.org:10.1016/S2666-5247(20)30172-5

63 Port, J. R. *et al.* SARS-CoV-2 disease severity and transmission efficiency is increased for airborne compared to fomite exposure in Syrian hamsters. *Nat Commun* **12**, 4985 (2021). https://doi.org:10.1038/s41467-021-25156-8

64 Qu, P. *et al.* Evasion of neutralizing antibody responses by the SARS-CoV-2 BA.2.75 variant. *Cell Host Microbe* **30**, 1518-1526 e1514 (2022). https://doi.org:10.1016/j.chom.2022.09.015

65 Wibmer, C. K. *et al.* SARS-CoV-2 501Y.V2 escapes neutralization by South African COVID-19 donor plasma. *Nature medicine* **27**, 622-625 (2021). https://doi.org:10.1038/s41591-021-01285-x

66 Planas, D. *et al.* Considerable escape of SARS-CoV-2 Omicron to antibody neutralization. *Nature* **602**, 671-675 (2022). https://doi.org:10.1038/s41586-021-04389-z

67 Bruel, T. *et al.* Longitudinal analysis of serum neutralization of SARS-CoV-2 Omicron BA.2, BA.4, and BA.5 in patients receiving monoclonal antibodies. *Cell Rep Med* **3**, 100850 (2022). https://doi.org:10.1016/j.xcrm.2022.100850

68 Planas, D. *et al.* Reduced sensitivity of SARS-CoV-2 variant Delta to antibody neutralization. *Nature* **596**, 276-280 (2021). https://doi.org:10.1038/s41586-021-03777-9

69 Bruel, T. *et al.* Serum neutralization of SARS-CoV-2 Omicron sublineages BA.1 and BA.2 in patients receiving monoclonal antibodies. *Nature medicine* **28**, 1297-1302 (2022). https://doi.org:10.1038/s41591-022-01792-5

70 Hoffmann, M. *et al.* The Omicron variant is highly resistant against antibody-mediated neutralization: Implications for control of the COVID-19 pandemic. *Cell* **185**, 447-456 e411 (2022). https://doi.org:10.1016/j.cell.2021.12.032

71 Matsuoka, K. *et al.* SARS-CoV-2 accessory protein ORF8 is secreted extracellularly as a glycoprotein homodimer. *J Biol Chem* **298**, 101724 (2022). https://doi.org:10.1016/j.jbc.2022.101724

72 Lin, X. *et al.* Unconventional secretion of unglycosylated ORF8 is critical for the cytokine storm during SARS-CoV-2 infection. *PLoS Pathog* **19**, e1011128 (2023). https://doi.org:10.1371/journal.ppat.1011128

73 Lin, X. *et al.* ORF8 contributes to cytokine storm during SARS-CoV-2 infection by activating IL-17 pathway. *iScience* **24**, 102293 (2021). https://doi.org:10.1016/j.isci.2021.102293

74 Wu, X. *et al.* Viral Mimicry of Interleukin-17A by SARS-CoV-2 ORF8. *mBio* **13**, e0040222 (2022). https://doi.org:10.1128/mbio.00402-22

75 Kee, J. *et al.* SARS-CoV-2 disrupts host epigenetic regulation via histone mimicry. *Nature* **610**, 381-388 (2022). https://doi.org:10.1038/s41586-022-05282-z

76 Zhang, Y. *et al.* The ORF8 protein of SARS-CoV-2 mediates immune evasion through down-regulating MHC-Iota. *Proc Natl Acad Sci U S A* **118** (2021). https://doi.org:10.1073/pnas.2024202118

77 Selvaraj, C. *et al.* SARS-CoV-2 ORF8 dimerization and binding mode analysis with class I MHC: computational approaches to identify COVID-19 inhibitors. *Brief Funct Genomics* (2023). https://doi.org:10.1093/bfgp/elac046

78 Pereira, F. Evolutionary dynamics of the SARS-CoV-2 ORF8 accessory gene. *Infect Genet Evol* **85**, 104525 (2020). https://doi.org:10.1016/j.meegid.2020.104525

79 DeRonde, S., Deuling, H., Parker, J. & Chen, J. Identification of a novel SARS-CoV-2 variant with a truncated protein in ORF8 gene by next generation sequencing. *Sci Rep* **12**, 4631 (2022). https://doi.org:10.1038/s41598-022-08780-2

989 80 de Vries, M. *et al.* A comparative analysis of SARS-CoV-2 antivirals characterizes 3CL(pro)
990 inhibitor PF-00835231 as a potential new treatment for COVID-19. *J Virol* **95** (2021).
991 https://doi.org:10.1128/JVI.01819-20
992

993

Acknowledgements

We thank Thomas M. Moran, Icahn School of Medicine at Mount Sinai, and Luis Martínez-Sobrido, Texas Biomedical Institute, for the kind gift of mouse monoclonal SARS-CoV N antibody 1C7, and Mehul Suthar, Emory School of Medicine, and Benjamin Pinsky, Stanford University, for the gift of the variants. We are grateful to the SARS-CoV-2 Assessment of Viral Evolution (SAVE) Program for critical input on our data. Histopathology of the murine nasopharynx was performed by Mark Alu and Branka Brukner Dabovic from the NYUMC Experimental Pathology Research Laboratory (RRID: SCR_017928). Both the Experimental Pathology Research Laboratory and the NYU Genome Technology Core are supported by NYU Cancer Center support grant P30CA016087 and by NYU Langone's Laura and Isaac Perlmutter Cancer Center and the Vectra Polaris multispectral scanner was purchased through a Shared Instrument Grant S10 OD021747. We are also grateful to the NYU Langone Antimicrobial-Resistant Pathogens (AMR) Program and thank Adriana Heguy and the team from the NYU Genome Technology Core for deep-sequencing of all viruses used in this study. Research was partially supported by the following grants from NIH/NIAID: R01AI143639 to M.D., K08AI141759 to M.B.O, R01AI143861 to K.M.K., DK093668 to K.C., and T32AI007180. None of the work with recombinant SARS-CoV-2 at NYU Grossman School of Medicine was funded by NIAID. Work was further supported by The Vilcek Institute of Graduate Biomedical Sciences, and by NYU Grossman School of Medicine Startup funds.

Author contributions

Bruno A. Rodriguez-Rodriguez: Conceptualization, Methodology, Validation, Formal analysis, Investigation, Writing – Original draft, Visualization. **Grace O. Ciabattoni:** Conceptualization, Methodology, Validation, Formal analysis, Investigation, Writing – Review & Editing, Visualization. **Ralf Duerr:** Conceptualization, Methodology, Validation, Formal analysis, Investigation, Writing – Review & Editing, Visualization. **Ana M. Valero-Jimenez:** Conceptualization, Methodology, Investigation, Writing – Review & Editing. Stephen T. Yeung: Methodology, Investigation, Writing – Review & Editing. **Keaton M. Crosse:** Conceptualization, Methodology, Investigation, Writing – Review & Editing. **Austin R. Schinlever:** Methodology, Investigation, Writing – Review & Editing. **Lucie Bernard-Raichon:** Conceptualization, Methodology, Investigation, Writing – Review & Editing. **Joaquin J. Rodriguez Galvan:** Methodology, Investigation, Writing – Review & Editing. **Marisa E. McGrath:** Methodology, Resources, Writing – Review & Editing. **Sanjay Vashee:** Methodology, Resources. **Yong Xue:** Methodology, Resources. **Cynthia Loomis:** Methodology, Supervision. **Kamal M. Khanna:** Methodology, Supervision, Funding Acquisition. **Kenneth Cadwell:** Methodology, Supervision, Funding Acquisition. **Ludovic Desvignes:** Methodology, Resources, Supervision, Writing – Review & Editing. **Matthew F. Frieman:** Conceptualization, Methodology, Resources, Supervision, Funding Acquisition, Writing – Review & Editing. **Mila B Ortigoza:** Conceptualization, Methodology, Formal analysis, Investigation, Writing – Original draft, Visualization, Supervision, Funding Acquisition. **Meike Dittmann:** Conceptualization, Methodology, Formal analysis, Investigation, Writing – Original draft, Visualization, Supervision, Funding Acquisition.

Competing Interests

The authors declare no competing interests.